Cavity-mediated two-qubit gate: Tuning to optimal performance with NISQ-era quantum simulations

Shreekanth S. Yuvarajan [1,*] Vincent Iglesias-Cardinale [1] David Hucul,[2] and Herbert F. Fotso [1,†]
[1]*Department of Physics, University at Buffalo SUNY, Buffalo, New York 14260, USA*
[2]*United States Air Force Research Laboratory, Rome, New York 13441, USA*

(Received 12 December 2025; accepted 27 October 2026; published 17 November 2026)

A variety of photon-mediated operations are critical to the realization of scalable quantum information processing platforms and their accurate characterization is essential for the identification of optimal regimes and their experimental realizations. Such light-matter interactions are often studied with a broad variety of analytical and computational methods that are constrained by approximation techniques or by computational scaling. Quantum processors present a new avenue to address these challenges. Here, we develop and implement an algorithm compatible with NISQ (noisy intermediate scale quantum) devices that allows a comprehensive characterization of cavity mediated two-qubit gates over a broad parameter space. In particular, we investigate the underlying quantum state transfer between the qubits, and illustrate its efficiency as a function of the detunings and couplings between the qubits and the cavity, and as a function of the damping factor of the cavity. Our algorithm is validated by a comparison with analytical results where applicable. The algorithm allows us to identify underexplored regimes of optimal performance, from which we report two insightful findings—one where we observe a state transfer fidelity of about 99% in the intermediate detuning regime, and the other where we observe a significant boost in fidelity with qubits that are moderately detuned from each other by coupling them unequally to a far-detuned cavity. Furthermore, we illustrate the breakdown of the rotating wave approximation as we approach the ultrastrong coupling and the deep-dispersive regimes. While the current paper addresses a system that only involves a few qubits and can be solved using classical numerical methods, the algorithm can be readily extended to study a variety of systems and processes in quantum information processing that employ cavity- or photon-mediated coupling between qubits, particularly larger systems such as many-emitter ensembles, cavity arrays, and multimode cavities, that are classically intractable.

DOI: 10.1103/mhhs-c3x9

I. INTRODUCTION

The optimization of light-matter interfaces arising in a variety of operations is key to the realization of scalable quantum platforms [1–7]. For instance, effective coupling enabling the implementation of quantum gates can be achieved between pairs or ensembles of qubits placed in a cavity [8–13]. However, the efficiency of such light-mediated operations will depend on specific parameters of the emitters and of the cavity, and their precise characterization is essential for effective experimental realizations. Such accurate characterization of light-matter interactions in various quantum information processing (QIP) applications plays an important role in guiding technological advancements and in understanding intriguing emergent behaviors. Analytical solutions of suitable models are often constrained by various unavoidable approximations that are made to keep the problem tractable [14–17]. Such approximations may for instance involve integrating out the bosonic modes and solving for the density matrix operator of the qubits [18–20]. They are often constrained in their validity to specific regions of parameter space and can easily lead to misleading spurious results. Alternatively, computational methods can be employed to tackle the problem. These numerical solutions, in addition to suffering from typical scaling issues when addressing quantum systems with classical computing algorithms, often involve an additional layer of abstraction between the model of the physical system and the classical algorithm.

Nascent quantum computers have brought about new possibilities for the simulation of quantum systems [21–26]. Although quantum processors are still in their infancy, quantum algorithms, even when solved on quantum simulators, offer a pathway to simulate quantum systems through a mapping that affords the user the capacity to directly track the dynamics of a quantum system.

Two-qubit gates can be performed through light-mediated interaction between qubits placed in a cavity, e.g., between quantum dots, superconducting qubits or atoms in a cavity [8–13]. To characterize and optimize these QIP operations, a variety of analytical and computational methods have been previously used. Furthermore, a number of initiatives have

*Contact author: shreekan@buffalo.edu
†Contact author: hffotso@buffalo.edu

Published by the American Physical Society under the terms of the Creative Commons Attribution 4.0 International license. Further distribution of this work must maintain attribution to the author(s) and the published article's title, journal citation, and DOI.

explored various methods to optimize this process using analytical and numerical approaches [27–35].

In this paper, we study the efficiency of this photon-mediated operation by implementing quantum circuits that are compatible with noisy intermediate-scale quantum (NISQ)-era systems. The algorithm solves the quantum optics model describing the dynamics of the system and allows us to reliably characterize the validity of conventional approximations that often inhibit analytical/numerical solutions. We focus on the case of a quantum state transfer and our approach allows us to assess the fidelity of the operation between two qubits and its dependence on various system parameters such as the emission frequencies of the qubits, the cavity frequency, the respective qubit couplings to the cavity, as well as the damping factor of the cavity. We examine the effect of the rotating wave approximation (RWA) on the state transfer operation. We are also able to access the dispersive regime without any need for a perturbative solution such as the Schrieffer-Wolff transformation (SWT).

An important consideration is that computational scaling remains an important hurdle in the adoption of quantum algorithm for many-particle systems. In particular, for systems involving bosonic degrees of freedom, this problem is exacerbated by the possible large number of excitations in one mode. However, for the problem at hand, as is the case in various light-matter processes in QIP, this concern is primarily alleviated by the fact that the system can be reasonably considered to be isolated during the timescale of the simulation. Additionally, as justified in Appendix I, we generally operate in a regime where the couplings and detunings between each qubit and the cavity are much smaller than the cavity frequency ($\leqslant 10\%$), ensuring that the energy nonconserving terms in the two-qubit quantum Rabi Hamiltonian do not appreciably populate higher cavity states. Therefore, the number of excitations in the entire system is limited and is capped by the preparation of the initial state (e.g., a single excitation, for one qubit in the excited state, the other in the ground state and an empty cavity), justifying the two-level approximation for the cavity. In this way, the simulation can be performed with only a handful of qubits (three qubits for two qubits in an ideal cavity, four qubits for two qubits in a cavity with a finite damping factor). The only exception to this is in Sec. VII where we examine the system in the ultrastrong coupling and deep-dispersive regimes, where the qubit-cavity couplings and detunings are not much smaller than the cavity frequency. In such cases, we expect appreciable population of higher cavity levels and accordingly model the cavity with a higher maximum occupation. It is clear from the problem size that this specific situation can be handled by exact diagonalization on a classical computer. However, in addition to its application presented in the current paper, the method utilized for the present studies could be readily generalized to larger problem sizes, including variations of cavity-mediated two-qubit gates with many radiation modes in the cavity. Also, the method is rather robust and intuitive in its implementation. For these reasons, we adopt and characterize a model that can be adapted to a variety of problems and systems, which on the one hand, can involve the identification of optimal operational regimes for high-performance gates on particular platforms, for example, spin [36], superconducting [37], or hybrid [38], and on the other, involve larger systems such as multimode cavities [39] or coupled cavity arrays [40]. Indeed, as an example for the latter, we recently examined the possibility of superradiance in a spectrally inhomogeneous ensemble of emitters using quantum circuits [41]. The subject of cavity mediated state transfer itself is of much interest experimentally [42,43]. More generally, the method proposed in the present paper can be extended to address broader efforts to simulate and optimize photon-mediated two-qubit gates and other relevant operations in quantum information processing that use light-matter interfaces [27–35].

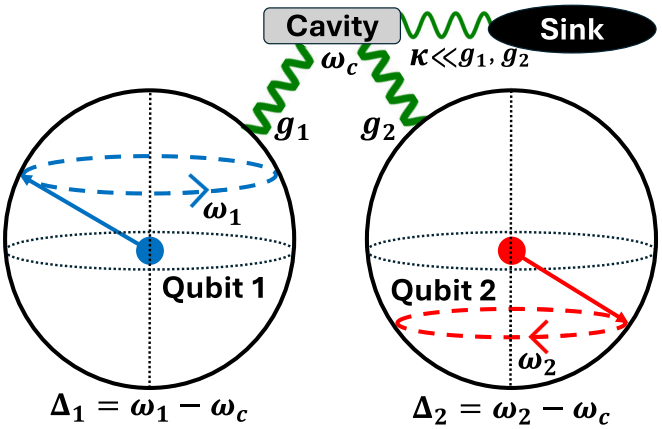


FIG. 1. Schematic description of a system of two qubits coupled through a cavity. Qubit 1 and Qubit 2 operate at frequencies $\omega_1 = \omega_c + \Delta_1$ and $\omega_2 = \omega_c + \Delta_2$, respectively, and are coupled to the cavity with respective coupling strengths g_1 and g_2. Δ_1 and Δ_2 are the detunings of Qubit 1 and Qubit 2, respectively, with the cavity that has a damping factor κ and is at frequency ω_c. The damping process is represented by the coupling of the cavity with a sink.

The rest of the paper is structured as follows. In Sec. II, we describe the model describing the system of interest and the associated Hamiltonian. In Sec. III, we present the procedure that we follow, starting with a mapping of the two-qubit extension of the quantum Rabi Hamiltonian onto a Hamiltonian of qubits, followed by the Trotter decomposition for the time evolution of the quantum state under the "qubitized" Hamiltonian, and then the quantum circuit that is used for this time evolution. We also discuss the systematic errors due to the Trotter decomposition of our Hamiltonian. In Sec. IV, we discuss our analysis for the transfer of the fully polarized state and present the effects of a finite damping parameter on the cavity. In Sec. V, we examine the state transfer operation when the two emitters have different coupling strengths to the cavity. In Sec. VI, we present our analysis of the state transfer for the superposition state. In Sec. VII, we discuss the rotating wave approximation and its regimes of validity. We end with our conclusions in Sec. VIII. The analytical solutions for a few special situations are shown in the Appendixes.

II. MODEL

We study the system that can be pictured schematically by Fig. 1. The figure describes a system of two qubits coupled through a cavity. While this iteration of the two-qubit gate can be treated with a classical computer, we use our quantum

algorithm that would be readily applicable to more complex cases beyond the capacity of classical hardware. Qubit 1 and Qubit 2 operate at frequencies $\omega_1 = \omega_c + \Delta_1$ and $\omega_2 = \omega_c + \Delta_2$, respectively, and are coupled to the cavity with respective coupling strengths g_1 and g_2. Δ_1 and Δ_2 are, respectively, the detunings of Qubit 1 and Qubit 2 with the cavity that has a damping factor κ and is at frequency ω_c. The damping process is represented by the coupling of the cavity with a sink. Such a system serves as a model for studying state transfer dynamics between the qubits for a variety of conditions.

In what follows, we will first consider the case of equal coupling strengths between the qubits and the cavity, i.e., $g_1 = g_2$ and discuss it extensively. We will later consider the case where the couplings are different in Sec. V. We will also focus the initial discussion on the case of an ideal cavity ($\kappa = 0$) before mentioning the case of finite damping in Sec. IV E.

For a perfect cavity, $\kappa = 0$, the system can be described by the two-qubit quantum Rabi Hamiltonian that extends the quantum Rabi Hamiltonian [44,45] to an ensemble, here, a pair of two-level systems corresponding to our qubits, placed inside a cavity. Its Hamiltonian is

$$\begin{aligned} H = {} & \frac{\hbar\omega_1}{2}\sigma_1^z + \frac{\hbar\omega_2}{2}\sigma_2^z + \hbar\omega_c a_c^\dagger a_c \\ & + \hbar g_1(a_c^\dagger\sigma_1^- + a_c\sigma_1^+ + a_c^\dagger\sigma_1^+ + a_c\sigma_1^-) \\ & + \hbar g_2(a_c^\dagger\sigma_2^- + a_c\sigma_2^+ + a_c^\dagger\sigma_2^+ + a_c\sigma_2^-). \end{aligned} \tag{1}$$

Here, ω_1, ω_2, and ω_c are, respectively, the frequencies of Qubit 1, Qubit 2, and the cavity. $a_c^\dagger$ and a_c are, respectively, the creation and annihilation operators for the radiation mode at the frequency ω_c. σ^z, $\sigma_i^- = |g_i\rangle\langle e_i|$, and $\sigma^+ = (\sigma^-)^\dagger$ are, respectively, the z-axis Pauli matrix, the lowering, and the raising operators for the two-level system, with $|g_i\rangle$ and $|e_i\rangle$ the ground and the excited states of Qubit i.

In general, the state of the system at time t can be written as

$$|\Psi(t)\rangle = \sum_l \alpha_l(t)\left|\Phi_1^l\right\rangle \otimes \left|\Phi_c^l\right\rangle \otimes \left|\Phi_2^l\right\rangle, \tag{2}$$

where $|\Phi_i^l\rangle$ with $i = 1,\ 2$ is the state of Qubit i, $|\Phi_c^l\rangle$ is the state of the cavity, and $\alpha_l(t)$ is a complex number. We have $|\Phi_i^l\rangle = |e_i\rangle$ or $|g_i\rangle$, $|\Phi_c^l\rangle = |0_c\rangle$ or $|1_c\rangle$, with $|0_c\rangle$ and $|1_c\rangle$ the ground and the first excited state of the cavity. Since each of the $|\Phi_j^l\rangle$ with $j = 1,\ 2,\ c$ lives in a two-dimensional space, the state of the system exists in an eight-dimensional space. Thus, the problem is not generally tractable analytically. There are, however, analytical solutions for special parameter sets, some of which we discuss later in the paper.

The goal of the quantum state transfer is to achieve the transfer of the state $|\Phi_1\rangle$ onto Qubit 2. Thus, the fidelity of the operation after time t is $F(t) = |\langle\Psi_{\text{target}}|\Psi(t)\rangle|^2$, with $|\Psi(0)\rangle = |\Phi_1 0_c g_2\rangle$ and $|\Psi_{\text{target}}\rangle = |g_1 0_c \Phi_2\rangle$. We use this quantity to examine the quantum state transfer operation, when the system is initialized by setting Qubit 1 in state $|\Phi_1(0)\rangle$ while Qubit 2 is in state $|\Phi_2(0)\rangle$ and the cavity is kept in its ground state. In all solutions presented in this work, $|\Phi_2(0)\rangle = |g\rangle$. We will show that although it is not in general possible to compute this quantity for all system parameters analytically, our quantum circuits allow for an extensive examination of the operation throughout the parameter space.

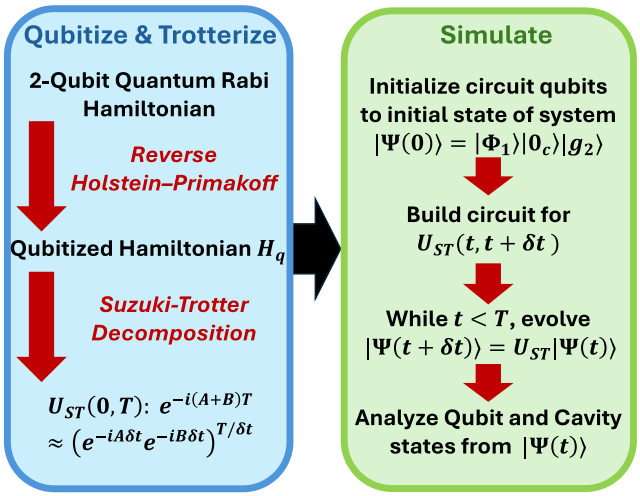


FIG. 2. Illustration of the approach to solve the problem through the implementation of a quantum circuit. The left-hand side depicts the analytical procedure of "qubitizing" the Hamiltonian, i.e., mapping the two-qubit quantum Rabi Hamiltonian on to a Hamiltonian with only qubits. This analytical component also includes the Trotter decomposition. The right-hand side highlights the steps of the quantum simulation to evolve the quantum state either on a quantum simulator or on a quantum processor.

III. METHODS

The overall solution is summarized in the flowchart shown in Fig. 2. The left-hand side of the figure depicts the analytical procedure of "qubitizing" the Hamiltonian, i.e., mapping the two-qubit quantum Rabi Hamiltonian on to a Hamiltonian with only qubits. This analytical component also includes the Trotter decomposition. The right-hand side of the figure highlights the steps of the quantum simulation to evolve the quantum state.

A. From two-qubit quantum Rabi to qubit Hamiltonian

Beginning with the Hamiltonian in Eq. (1) and setting $\hbar = 1$, we apply the transformation [46]

$$\begin{aligned} \sigma_i^z &= -Z_i, \\ \sigma_i^+ &= \tfrac{1}{2}(X_i - \mathrm{i}Y_i), \\ \sigma_i^- &= \tfrac{1}{2}(X_i + \mathrm{i}Y_i), \\ a_c^\dagger \equiv \sigma_c^+ &= \tfrac{1}{2}(X_c - \mathrm{i}Y_c), \\ a_c \equiv \sigma_c^- &= \tfrac{1}{2}(X_c + \mathrm{i}Y_c). \end{aligned} \tag{3}$$

Here, X, Y, Z, and I are Pauli operators on the qubits and we use the subscript c to identify the qubit corresponding to the cavity. This mapping of the cavity mode operators to Pauli operators is enabled by constraining the total excitation in the system to remain equal to 1, which is reasonable when the system is initially prepared with just one excitation, is isolated, and is operated away from the ultrastrong or deep-dispersive regimes, as discussed in the introduction and justified in Appendix I. In Sec. VII, we use a four-level cavity modeled using a binary encoding [47]. Plugging the qubit operators above into the Hamiltonian in Eq. (1), we get the "qubitized"

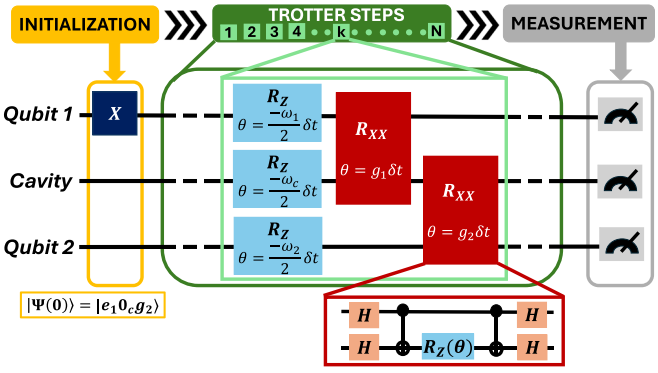


FIG. 3. Quantum circuit for the time evolution of the initial state of a two-qubit system in a cavity under the two-qubit quantum Rabi Hamiltonian. The circuit includes three qubits. The second qubit in the circuit represents the cavity while the first and the third represent Qubit 1 and Qubit 2, respectively, in our two-qubit quantum Rabi Hamiltonian.

Hamiltonian (see Appendix B):

$$H_q = -\frac{\omega_1}{2}Z_1 - \frac{\omega_2}{2}Z_2 + \frac{\omega_c}{2}(I_c - Z_c) + g_1(X_cX_1) + g_2(X_cX_2). \tag{4}$$

Since we are interested in evolving the system in time, we use the Trotter decomposition to break the time-evolution operator into its action over finite time steps δt:

$$U(0,t) \approx (\mathrm{e}^{-\mathrm{i}H_0\delta t}\mathrm{e}^{-\mathrm{i}H_{\mathrm{int}}\delta t})^{t/\delta t}, \tag{5}$$

so that

$$U(t, t+\delta t) \approx \mathrm{e}^{-\mathrm{i}H_0\delta t}\mathrm{e}^{-\mathrm{i}H_{\mathrm{int}}\delta t}, \tag{6}$$

with

$$H_0 = -\frac{\omega_1}{2}Z_1 - \frac{\omega_2}{2}Z_2 + \frac{\omega_c}{2}(I_c - Z_c), \tag{7}$$

$$H_{\mathrm{int}} = g_1(X_cX_1) + g_2(X_cX_2). \tag{8}$$

B. Quantum circuit and systematic error

With the appropriate initial state, the quantum state of the system of qubits is evolved in time using the above mentioned Trotter decomposition that breaks the time evolution into terms that can be simulated with gates on appropriate qubits. The initialization and the time evolution are illustrated on the right-hand side of Fig. 2. The number of time steps is chosen to minimize the systematic error while allowing simulations up to multiple relaxation times of the individual emitters. The quantum computation is performed with a Python code using the Qiskit library [48].

The quantum circuit is shown schematically in Fig. 3. The figure shows three qubits, the second of which represents the cavity while the first and the third represent Qubit 1 and Qubit 2, respectively, in our two-qubit quantum Rabi Hamiltonian qubitized into Eq. (4).

In order to characterize the systematic error due to finite time-step discretization, we analytically estimate and analyze this error through the simulations on the quantum circuits of the Hamiltonian H_q. To help highlight key timescales involved in H_q, we transform it to the frame rotating at the cavity

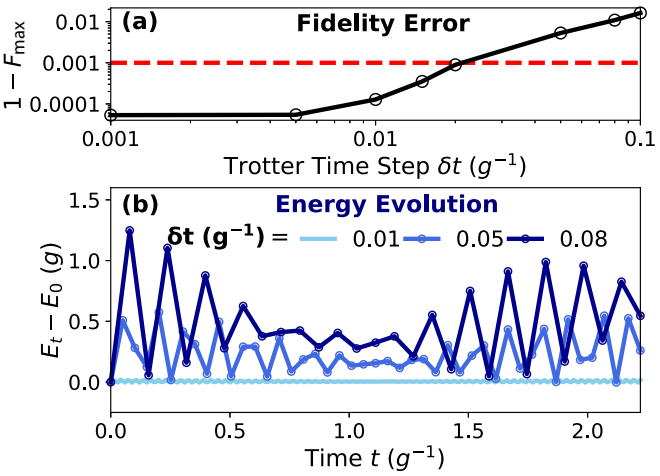


FIG. 4. Illustration of the systematic error in the time evolution due to the Trotter decomposition. (a) Difference with ideal fidelity, $1 - F_{\max}$, for the transfer of the polarized state from Qubit 1 to Qubit 2 as a function of the Trotter time step δt. The dashed line represents the target of $1 - F_{\max} \leqslant 0.001$. (b) Evolution of the total energy in the system as a function of time for $\delta t = 0.01\, g^{-1}$, $\delta t = 0.05\, g^{-1}$, and $\delta t = 0.08\, g^{-1}$.

frequency (see Appendix F).

$$\begin{aligned} H_q^{\mathrm{cavity}} = \sum_{i=1,2} & -\frac{\Delta_i}{2}Z_i + \frac{g_i}{2}(X_cX_i + Y_cY_i) \\ & + \frac{g_i}{2}\cos(2\omega_c t)(X_cX_i - Y_cY_i) \\ & + \frac{g_i}{2}\sin(2\omega_c t)(X_cY_i + \mathrm{i}Y_cX_i). \end{aligned} \tag{9}$$

By examining this form of the Hamiltonian, we can estimate that the leading order error in the time evolution operator $U(t, t+\delta t)$, due the Trotter decomposition satisfies (see Appendix F):

$$\epsilon \sim \delta t^2(g_1\Delta_1 + g_2\Delta_2 + g_1g_2). \tag{10}$$

For N total time steps, an upper bound on the time step δt, for a desired total accumulated error ϵ_{tot} in a simulation from time $t_0 = 0$ to time $T = N\delta t$ is given by

$$\delta t \sim \frac{\epsilon_{\mathrm{tot}}}{T(g_1\Delta_1 + g_2\Delta_2 + g_1g_2)}. \tag{11}$$

We benchmark our simulations by choosing a time step that produces an error in fidelity, $1 - F \leqslant 0.001$ for the corresponding complete state transfer operation (resonant or dispersive). This translates to a Trotter error $\epsilon_{\mathrm{tot}} \equiv \sqrt{1-F} = 0.0316$ [49,50].

We consider for further analysis of the systematic error, the case of emitters resonant with the cavity $\Delta_1 = \Delta_2 = 0$ and where $g_1 = g_2 = g$. The transfer of the fully polarized state from Qubit 1 to Qubit 2 occurs after time $T = \pi/\sqrt{2}g$ and the desired fidelity requires

$$\delta t \sim 0.015\, g^{-1}. \tag{12}$$

In Fig. 4, we characterize the systematic error due to the Trotter discretization of the time axis by simulating the resonant transfer of the polarized state discussed above. The figure shows in panel (a) the fidelity error as a function of

the time step δt. The dashed red line corresponds to our target error in the fidelity. Panel (b) shows the difference between the actual total energy in the system and the computed total energy, as a function of time for different choices of the time step. We see a clear suppression of the variation in the total energy of the system by reducing δt. We also note that the symmetry in the dynamics of the system is reflected in the energy deviation as a function of time, which is lowest when the excitation is most evenly distributed (at $t = T/2$) and highest when it is solely held in one of the qubits (at $t = 0, T$).

In what follows, with the exception of Sec. V, we mostly consider the case of $g_1 = g_2 = g$. We separately examine the case of the transfer of the fully polarized state and the case of the superposition state. All simulations are performed with $g = 1$, thus setting our energy and time units by the coupling strength between the cavity and the qubits. Except for the simulation results in Figs. 8(c), 8(d), and 11(a), all simulations are performed with cavity frequency $\omega_c = 100g$. The simulations are performed using an ideal classical simulator. In Appendix K, we discuss the performance of the circuit for the resonant transfer of the quantum state from Qubit 1 to Qubit 2 on a current quantum processor (ibm_marrakesh [51], which is one of the IBM Heron r2 quantum processors). The results match that of the ideal simulator for moderate times but begin to deviate at longer times due to factors such as two-qubit gate fidelity and potentially suboptimal qubit allocation and circuit execution on the shared platform. We expect better results with optimized settings or on dedicated platforms.

In order to characterize particular subsystems, and specific interactions between them, we construct the density matrix $\rho(t) = |\Psi(t)\rangle\langle\Psi(t)|$ for the global system state $|\Psi(t)\rangle$.

To obtain the reduced density matrices of Qubit 1, Qubit 2, or the cavity, we trace out Qubit 2 and cavity, Qubit 1 and cavity, or Qubit 1 and Qubit 2, respectively. We can extract the effective coupling strength between a pair of subsystems (coherences) by tracing out the third subsystem to build a reduced density matrix (4×4) representing the pair. Such reduced density matrices are written as

$$\rho_i(t) = \mathrm{Tr}_{j,k}[\rho(t)], \tag{13}$$

$$\rho_{ij}(t) = \mathrm{Tr}_k[\rho(t)], \tag{14}$$

where $(i, j, k) \in \{(1, c, 2), (2, c, 1), (c, 1, 2)\}$. From $\rho_i(t)$, one can get the populations and phases of the qubits and cavity as $|c_e|^2$ and $\arg(c_e c_g^*)$, respectively. From $\rho_{ij}(t)$, one can get the coherence between subsystems i and j as $\arg(c_{e0} c_{g1}^*)$ for $i, j = 1(2), c$ and $\arg(c_{eg} c_{ge}^*)$ for $i, j = 1, 2$.

We obtain analytical expressions where tractable for the time dynamics of our model using the RWA version of the two-qubit quantum Rabi model, also known as the Tavis-Cummings model [52]:

$$H^{\mathrm{RWA}} = \frac{\hbar\omega_1}{2}\sigma_1^z + \frac{\hbar\omega_2}{2}\sigma_2^z + \hbar\omega_c a_c^\dagger a_c + \hbar g_1(a_c^\dagger\sigma_1^- + a_c\sigma_1^+) + \hbar g_2(a_c^\dagger\sigma_2^- + a_c\sigma_2^+). \tag{15}$$

IV. TRANSFER OF THE POLARIZED STATE

Except for select special cases, characterizing the state transfer between the two qubits is rather nontrivial in general. We first consider the case of a polarized state in Qubit 1 to be transferred onto Qubit 2.

A. Qubits resonant with the cavity

For the case of qubits that are resonant with the cavity, as we will discuss in Sec. VII, our simulations coincide with the RWA for which an analytical solution is achievable. Thus, we can use this RWA result to benchmark the quantum circuit results. Indeed, for $\Delta_1 = \Delta_2 = 0$, the RWA Hamiltonian [Eq. (15)] in the frame rotating at the cavity frequency, and with $g_1 = g_2 = g$ is given by

$$H = g(a_c^\dagger\sigma_1^- + a_c\sigma_1^+ + a_c^\dagger\sigma_2^- + a_c\sigma_2^+). \tag{16}$$

For the system with a single excitation (only one of the qubits in the excited state or only the first excited state of the cavity occupied), the dynamics is restricted to the subspace spanned by the set of three states: $\{|e_1 0_c g_2\rangle, |g_1 1_c g_2\rangle, |g_1 0_c e_2\rangle\}$. With the initial state $|\Psi(0)\rangle = |e_1 0_c g_2\rangle$, the time-dependent state under the Hamiltonian in Eq. (16) is (see Appendix C)

$$|\Psi(t)\rangle = \left(\frac{1+\cos(\sqrt{2}gt)}{2}\right)|e_1 0_c g_2\rangle - \left(\frac{i\sin(\sqrt{2}gt)}{\sqrt{2}}\right)|g_1 1_c g_2\rangle + \left(\frac{\cos(\sqrt{2}gt)-1}{2}\right)|g_1 0_c e_2\rangle. \tag{17}$$

From the above equation, it is easy to see that complete state transfer from Qubit 1 to Qubit 2 occurs at

$$t_f = \frac{\pi}{\sqrt{2}g}. \tag{18}$$

B. Dispersive regime

For qubits in the dispersive regime, the effective Hamiltonian in the RWA and in the frame rotating at the cavity frequency can be obtained through a Schrieffer-Wolf transformation to be [53]

$$H_{\mathrm{eff}} = \frac{g^2}{\Delta}\left(\sigma_1^z + \sigma_2^z\right) + \frac{g^2}{\Delta}\left(\sigma_1^+\sigma_2^- + \sigma_1^-\sigma_2^+\right). \tag{19}$$

This Hamiltonian in the dispersive regime eliminates the cavity and hence, the dynamics is constrained to the subspace spanned by the states: $\{|e_1 g_2\rangle, |g_1 e_2\rangle\}$. With the excitation initially in Qubit 1, we get

$$|\Psi(t)\rangle = \tfrac{1}{2}\left(1 + e^{-2ig^2 t/\Delta}\right)|e_1 g_2\rangle + \tfrac{1}{2}\left(-1 + e^{-2ig^2 t/\Delta}\right)|g_1 e_2\rangle. \tag{20}$$

The time for complete state transfer ($|e_1 g_2\rangle \to |g_1 e_2\rangle$) in the dispersive regime is obtained as

$$t_f' = \frac{\pi\Delta}{2g^2}. \tag{21}$$

C. General solution

Figure 5 shows the solution with our quantum circuit for the general Hamiltonian (without the RWA) for different

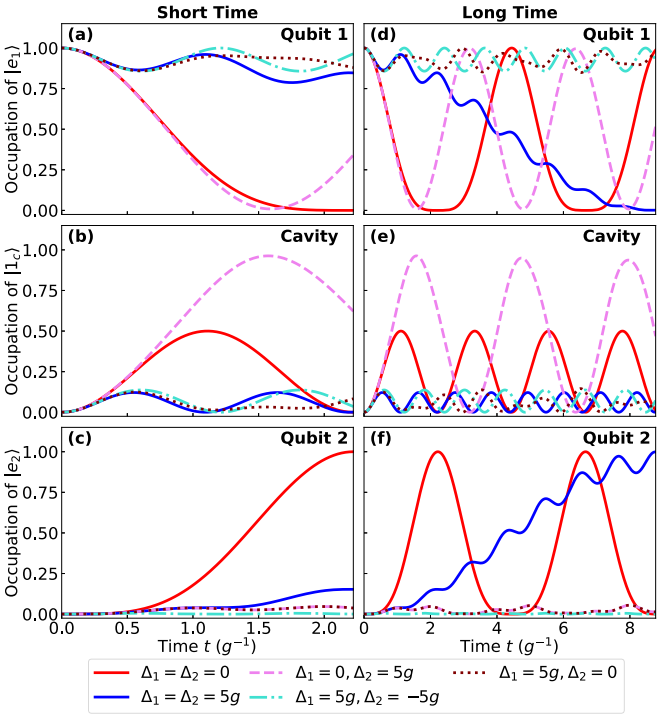


FIG. 5. Evolution of the occupation of the qubits and the cavity excited states as a function of time. The system is initially in the state with Qubit 1 in its excited state and Qubit 2 and the cavity in their ground states. Panels (a)–(c) show short time dynamics up to the time for first resonant state transfer t_f. Panels (d)–(f) show long time dynamics up to the time for the first dispersive state transfer $t_f'(\Delta = 5g)$.

combinations of the detunings Δ_1 and Δ_2 selected to illustrate the variety of behaviors in the system. The figure presents the occupation of the excited states of Qubit 1 and Qubit 2 and of the first excited state of the cavity as a function of time. The left panels show the evolution up to a time t_f at which the complete state transfer would occur in the resonant case. The right panels show the evolution of the system for longer times. The resonant case is represented by the solid red lines, which at $t = t_f$, shows complete state transfer from Qubit 1 to Qubit 2 (with a global phase shift of π). Also, at $t = t_f/2$, the cavity reaches its maximum occupation, which is equal to half the total excitation in the system, in agreement with the analytical expression of Eq. (17).

The detuning value of $\Delta = 5g$ is chosen to illustrate the dynamics as we approach the dispersive regime ($\Delta \gg g$). In general, it is observed that increased detuning suppresses excitation transfer. However, the symmetric detuning configuration, where the qubits are resonant with each other but detuned with the cavity (illustrated in the figure by $\Delta_1 = \Delta_2 = 5g$), shows a slow but near-complete transfer at a longer time, through effective qubit-qubit virtual coupling without ever significantly populating the excited state of the cavity.

The configuration in which Qubit 1 is resonant with the cavity and Qubit 2 is detuned (illustrated in the figure by $\Delta_1 = 0$ and $\Delta_2 = 5g$), shows coherent population oscillations between Qubit 1 and cavity, but only draws a feeble oscillatory response from Qubit 2. The complementary configuration in which Qubit 1 is detuned from the cavity while Qubit 2 is resonant with the cavity (in the figure, $\Delta_1 = 5g$ and $\Delta_2 = 0$), shows weak oscillations in all subsystems. This is because even though Qubit 2 is resonant with the cavity, the system initially has the excitation in Qubit 1, which is detuned from the cavity. The configuration in which both qubits are oppositely detuned (illustrated in the figure by $\Delta_1 = 5g$ and $\Delta_2 = -5g$) shows weak oscillations between Qubit 1 and cavity, and even weaker oscillations in Qubit 2 excited-state occupation, due to the initial state of the system as mentioned above.

D. Fidelity

To characterize the quantum state transfer operation at time t, we use the fidelity defined by

$$F(t) = |\langle \Psi_{\text{target}} | \Psi(t) \rangle|^2, \tag{22}$$

with $|\Psi(0)\rangle = |e_1 0_c g_2\rangle$ and $|\Psi_{\text{target}}\rangle = |g_1 0_c e_2\rangle$. To analyze the dependence of the efficiency on the parameters of the system, we solve the problem with our quantum circuit for a broad set of detuning values, evolving the system up to long times, and then extracting the maximum achieved fidelity. A figure of merit for the state transfer operation is then the maximum fidelity achieved, as well as the time to achieve this value. Figure 6 presents through a heat map the maximum fidelity in panel (a), and the time to achieve this maximum fidelity in panel (b), as a function of the detunings Δ_1 and Δ_2 between Qubit 1 and the cavity and between Qubit 2 and the cavity, respectively. We observe that maximal fidelity is achieved for both qubits resonant with the cavity and with both qubits resonant with each other in the dispersive regime [diagonal values in Fig. 6(a)]. The fidelity is lowered as the frequencies of Qubit 1 and Qubit 2 are tuned away from each other [off-diagonal values in Fig. 6(a)]. In panel (b), we observe that the maximal fidelity achieved for $\Delta_1 = \Delta_2 \gg g$ (dispersive regime) is achieved over longer times [at $t_f'(\Delta)$] than for both Qubits resonant with the cavity (at t_f). In the intermediate regime ($g < \Delta_1 = \Delta_2 < 5g$), we observe maximal fidelity that is achieved over much longer times. Panel (c) shows further characterization of the long time dynamics through the occupation of the excited state of Qubit 2. It clearly indicates that the maximum fidelity is achieved over a long timescale in the intermediate regime, where complete state transfer is approached through a growing envelope of oscillations in the occupation of the excited state, reaching $F \approx 99\%$. We analytically characterize the time-dependent fidelity in the intermediate regime (see Appendix D) and find a close agreement with simulation data. As seen in the last two terms of Eq. (23), the oscillations are characterized by a frequency $\Omega = \sqrt{\Delta^2 + 8g^2}$ and an envelope frequency Δ, with $\Delta_1 = \Delta_2 = \Delta$:

$$\begin{aligned} F(t) = \frac{1}{4}\Bigg[1 + \frac{1}{2}\left(1 + \frac{\Delta^2}{\Omega^2}\right) + \frac{1}{2}\left(1 - \frac{\Delta^2}{\Omega^2}\right)\cos(\Omega t) \\ - 2\cos\left(\frac{\Delta}{2}t\right)\cos\left(\frac{\Omega}{2}t\right) \\ - \frac{2\Delta}{\Omega}\sin\left(\frac{\Delta}{2}t\right)\sin\left(\frac{\Omega}{2}t\right)\Bigg]. \end{aligned} \tag{23}$$

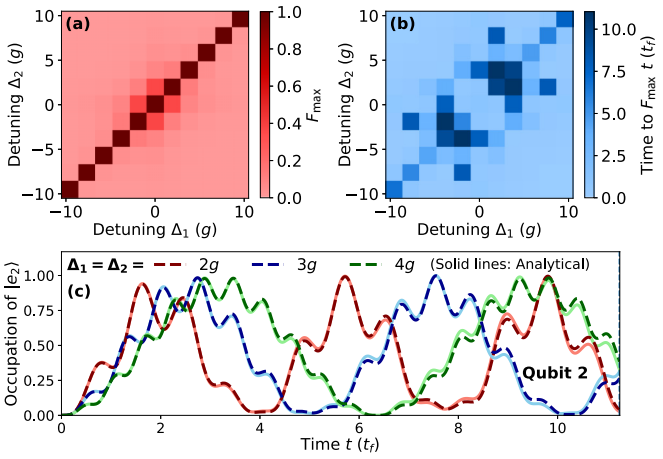


FIG. 6. (a) Heat map indicating the maximum achieved transfer fidelity $F_{\max}$ as a function of detuning configurations. The resonant and symmetrically detuned configurations ($\Delta_1 = \Delta_2$) form the diagonal in the fidelity heat map and show complete state transfer, through different mechanisms. Maximum fidelity rapidly drops in value with increased detuning asymmetry. (b) Heat map illustration of the time taken to achieve $F_{\max}$ as a function of the detuning configurations. The resonant configuration achieves complete transfer early (at $t = t_f$). The dispersive configurations ($\Delta_1 = \Delta_2 \gtrsim 5g$) achieve complete transfer over a longer time $t'_f(\Delta)$. The intermediate configurations ($\Delta_1 = \Delta_2 < 5g$) achieve transfer through a growing envelope like phenomenon over much longer times. Note the subtle asymmetry in darkness along the diagonal, between positive and negative equal detuning configurations (an effect missed by the RWA as discussed in Sec. VII). (c) Occupation of the excited state of Qubit 2 as a function of time for a set of detunings in the intermediate regime. The dashed lines represent simulation data, and the lighter solid lines represent their corresponding analytical forms given by Eq. (23). (For the setup in this subsection, fidelity is equivalent to the occupation of the excited state of Qubit 2.)

E. State transfer via a damped cavity

A realistic cavity is not perfect and is subject to photon loss through cavity leakage. In this scenario, the pair of qubits and the cavity form an open system whose time evolution is described by the Lindblad master equation:

$$\frac{d}{dt}\rho = \mathcal{L}_H(\rho) + \mathcal{L}_D(\rho), \tag{24}$$

where ρ is the density matrix of the Qubit 1-cavity-Qubit 2 system, and the Liouvillians $\mathcal{L}_H(\rho) = -\mathrm{i}[H, \rho]/\hbar$ and $\mathcal{L}_D(\rho) = \kappa a \rho a^\dagger - \kappa\{a^\dagger a, \rho\}/2$ correspond to unitary evolution and dissipation, respectively. The solution to Eq. (24) is $\rho(t) = \mathrm{e}^{(\mathcal{L}_H + \mathcal{L}_D)t}\rho(0)$, which, over a small time step δt in the Trotter approximation can be written as

$$\rho(t + \delta t) \approx \mathrm{e}^{\mathcal{L}_D \delta t}\mathrm{e}^{\mathcal{L}_H \delta t}\rho(t), \tag{25}$$

with $\mathrm{e}^{\mathcal{L}_H \delta t}(\rho) = U\rho U^\dagger = \rho'$, where $U = \mathrm{e}^{-\mathrm{i}H\delta t}$, and as shown in Appendix G, $\mathrm{e}^{\mathcal{L}_D \delta t}(\rho')$ can be expressed in the Kraus representation as $\sum_i \Omega_i \rho' \Omega_i^\dagger$. This allows the quantum circuit to be decomposed into a unitary evolution layer and an amplitude damping layer [54] as shown in Fig. 12. The arrangement uses an ancillary damping qubit, called the sink, which draws population out of the cavity at a rate κ. The sink is reset to $|0\rangle$ before each Trotter step and measured after it, to ensure a "one-way" flow of population from the cavity to the sink.

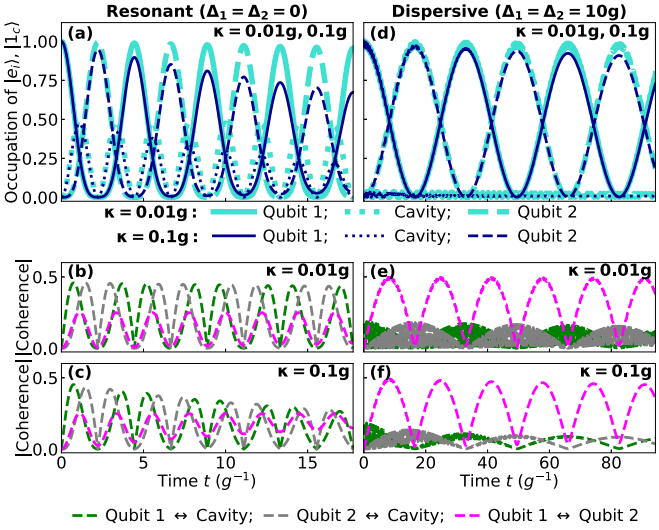


FIG. 7. Evolution as a function of time of the excited state occupation of the qubits and the cavity for both qubits resonant with the cavity [panel (a)], and for both qubits resonant with each other in the dispersive regime [panel (d)]. Evolution as a function of time of the coherences between pairs of subsystems, when the cavity is damped by a factor $\kappa = 0.01g$ [panel (b)] for the resonant case and [panel (e)] for the dispersive case, $\kappa = 0.1g$ [panel (c)] for the resonant case and [panel (f)] for the dispersive case.

Figure 7 shows the dynamics of the system with qubits resonant with the cavity and with qubits in the dispersive regime for different values of the damping constant. Panel (a) shows the occupation as a function of time of the excited states of the qubits and the cavity for damping rate $\kappa = 0.01g$ and for $\kappa = 0.1g$ when the qubits are resonant with the cavity. Panel (d) shows the same quantities for qubits in the dispersive regime with $\Delta_1 = \Delta_2 = 10g$. We observe that in the resonant configuration, the system loses its overall excitation gradually at a rate proportional to the damping coefficient κ. However, for the dispersive configuration, for the same κ, we observe a much slower damping, owing to the transfer in this regime being less affected by the cavity loss as it is only virtually populated. In the lower panels, the figure shows the coherences corresponding to the coupling of different pairs of subsystems. The figure clearly shows that the coherence between Qubit 1 and Qubit 2 [magenta dashed line in panels (b), (c), (e), and (f)] remains high in amplitude for the dispersive regime independently of the damping rate. Note also the suppression of the coherences between the qubits and the cavity (green and dark-gray dashed lines) in the dispersive regime.

V. TRANSFER BETWEEN QUBITS WITH DIFFERENT COUPLING STRENGTHS TO THE CAVITY

Here, we simulate the transfer of the fully polarized state from Qubit 1 to Qubit 2 for the case of unequal coupling strengths between the qubits and cavity, for the resonant and dispersive configurations.

A. Qubits resonant with cavity

Here, the time evolution of the system in the single excitation subspace spanned by the set of three states, $\{|e_1 0_c g_2\rangle, |g_1 1_c g_2\rangle, |g_1 0_c e_2\rangle\}$, is described by the quantum state (see Appendix C)

$$|\Psi(t)\rangle = \frac{g_1^2 \cos\left(\sqrt{g_1^2+g_2^2}t\right)+g_2^2}{g_1^2+g_2^2}|e_1 0_c g_2\rangle - \frac{\mathrm{i}g_1 \sin\left(\sqrt{g_1^2+g_2^2}t\right)}{\sqrt{g_1^2+g_2^2}}|g_1 1_c g_2\rangle + \frac{g_1 g_2\left(\cos\left(\sqrt{g_1^2+g_2^2}t\right)-1\right)}{g_1^2+g_2^2}|g_1 0_c e_2\rangle. \quad (26)$$

One can see that the maximum occupation probability of the excited state of Qubit 2 is

$$\max(P_2) = \left(\frac{g_1 g_2}{g_1^2+g_2^2}\left(\cos\left(\sqrt{g_1^2+g_2^2}t\right)-1\right)\right)^2. \quad (27)$$

This is equal to 1 only when $g_1 = g_2$ and $t = \frac{\pi}{\sqrt{g_1^2+g_2^2}} + 2n\pi$. Therefore, with unequal couplings, complete state transfer does not occur even if the qubits are resonant with the cavity.

B. Dispersive regime

For the dispersive configuration, with $\Delta_1 = \Delta_2$, the effective Hamiltonian in the RWA and in the frame rotating at the cavity frequency is obtained through a Schrieffer-Wolff transformation to be [53]

$$H_{\mathrm{eff}} = \sum_{i=1}^{2}\frac{g_i^2}{\Delta}\sigma_i^z + \sum_{i\neq j}\frac{g_i g_j}{2\Delta}(\sigma_i^+\sigma_j^- + \sigma_i^-\sigma_j^+). \quad (28)$$

The time evolution of the system in the single excitation subspace now spanned by two states, $\{|e_1 g_2\rangle, |g_1 e_2\rangle\}$, is described by the quantum state [53]

$$|\Psi(t)\rangle = \left(1+\frac{g_2^2}{g_1^2+g_2^2}\left(\mathrm{e}^{-\mathrm{i}t\left(g_1^2+g_2^2\right)/\Delta}-1\right)\right)|e_1 g_2\rangle + \frac{g_1 g_2}{g_1^2+g_2^2}\left(\mathrm{e}^{-\mathrm{i}t\left(g_1^2+g_2^2\right)/\Delta}-1\right)|g_1 e_2\rangle. \quad (29)$$

Here, the maximum occupation probability of the excited state of Qubit 2 is

$$\max(P_2) = \left(\frac{g_1 g_2}{g_1^2+g_2^2}\left(\mathrm{e}^{-\mathrm{i}t(g_1^2+g_2^2)/\Delta}-1\right)\right)^2. \quad (30)$$

This is equal to 1 only when $g_1 = g_2$ and $t = \frac{\pi\Delta}{g_1^2+g_2^2} + 2n\pi$. Therefore, with unequal couplings, complete state transfer does not occur in the dispersive regime.

In Fig. 8, panel (a) illustrates the drop in fidelity for the resonant state transfer of the polarized state as the ratio g_2/g_1 deviates from 1. $F_{\max} \sim 1$ when $g_2/g_1 = 1$, and is <1 otherwise, in agreement with the analytical expressions in Eqs. (27) and (30). Panel (b) shows the maximum state transfer fidelity as a function of qubit detunings when $g_2/g_1 = 4$. The state

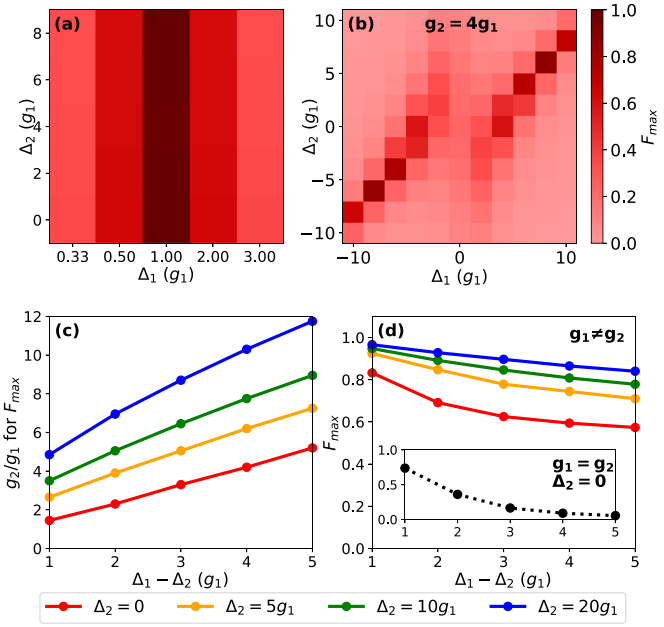


FIG. 8. (a) Heat map depicting the maximum achieved transfer fidelity $F_{\max}$ for qubits resonant and equally detuned with the cavity as a function of the ratio of couplings g_2/g_1 for the transfer of the fully polarized state in Qubit 1. (b) Heat map showing $F_{\max}$ as a function of qubit detunings Δ_1 and Δ_2 for $g_2/g_1 = 4$. (c) Ratio of couplings g_2/g_1 required to produce maximum transfer fidelity $F_{\max}$ as a function of detunings between the qubits, for a range of detunings between the qubits and the cavity. (d) Maximum transfer fidelity $F_{\max}$ as a function of detunings between the qubits, for a range of detunings between the qubits and the cavity, when the qubits are coupled to the cavity at the optimum ratio g_2/g_1 from panel (c). The inset shows the fidelity as function of detuning between the qubits when the qubits are equally coupled to the cavity and are near resonant with it. [In panels (c) and (d), the cavity frequency was accordingly increased to ensure $g_2 \ll \omega_c$ so that the two-level cavity is appropriate.]

transfer is generally poor, including along the diagonal, representing the resonant and equally detuned ($\Delta_1 = \Delta_2$) qubit configurations, due to the inequality in coupling. However, some off-diagonal cells show a higher state transfer fidelity. These cells correspond to favorable detuning combinations that compensate for the inequality in couplings by minimizing the difference between their "individual" qubit-cavity Rabi frequencies to give $\Omega_i = \sqrt{g_i^2+\Delta_i^2}$ such that $\Omega_1 \sim \Omega_2$. Such an interplay can be leveraged to efficiently couple qubits that are moderately detuned, often due to device/materials imperfections [55]. Panel (c) shows the ratio of couplings g_2/g_1 required to achieve maximum fidelity $F_{\max}$ as a function of qubit-qubit detuning $\Delta_1 - \Delta_2$, and also as a function of Qubit 2-cavity detuning Δ_2 for the transfer of the polarized state from Qubit 1 to Qubit 2. Panel (d) shows the maximum fidelity achieved as a function of $\Delta_1 - \Delta_2$ and Δ_2. We see that it is most efficient to couple the qubits unequally to a far-detuned cavity. This can be understood by considering that in this semidispersive regime, where one qubit is moderately detuned and the other is far detuned, the former populates the cavity appreciably, while the latter dispersively absorbs

excitation from it at a closely-matched effective rate. Indeed, with $\Delta_2 = 20g_1$, we get $F_{\max}$ between 97% and 84% for $\Delta_1 - \Delta_2$ between g_1 and $5g_1$. In comparison, the inset in panel (d) shows that the maximum fidelity is much lower and rapidly deteriorates with increasing $\Delta_1 - \Delta_2$ when the qubits are equally coupled to the cavity ($g_1 = g_2$), and near resonant with it.

VI. TRANSFER OF SUPERPOSITION STATE

The quantum circuits can be used to characterize the transfer of an arbitrary quantum state, including a superposition of the excited and ground state i.e., $|\Phi_1\rangle = \alpha|e_1\rangle + \beta|g_1\rangle$, with α and β complex numbers. For illustration, we focus here on the example of an equal superposition of the ground state and the excited state in Qubit 1 ($|\alpha| = |\beta| = 1/\sqrt{2}$).

A. Qubits resonant with the cavity

For qubits that are resonant with the cavity, the model for the transfer of a superposition state requires that we expand the allowed subspace to the space spanned by the four-state set $\{|e_1 0_c g_2\rangle, |g_1 1_c g_2\rangle, |g_1 0_c e_2\rangle, |g_1 0_c g_2\rangle\}$.

We note that the state $|g_1 0_c g_2\rangle$ is unaffected by the Tavis-Cummings Hamiltonian dynamics, rendering it a dark state. This, along with the linearity of the evolution operator $U(t)$, enables us to write the time-evolved state of the system as

$$|\Psi(t)\rangle = \alpha|\Psi_g(t)\rangle + \beta|\Psi_e(t)\rangle \tag{31}$$

$$= \alpha|\Psi_g(0)\rangle + \beta(U(t)|\Psi_e(0)\rangle) \tag{32}$$

$$= \alpha|g_1 0_c g_2\rangle + \beta(U(t)|e_1 0_c g_2\rangle), \tag{33}$$

where α and β are complex numbers. Essentially, $|\Psi(t)\rangle$ for the superposition state only depends on the evolution of the excited component since the ground-state component is preserved. Replacing $|\Psi_e(t)\rangle$ with Eq. (17), we get

$$|\Psi(t)\rangle = \alpha|g_1 0_c g_2\rangle + \beta\Bigg[\left(\frac{1+\cos(\sqrt{2}gt)}{2}\right)|e_1 0_c g_2\rangle - \left(\frac{i\sin(\sqrt{2}gt)}{\sqrt{2}}\right)|g_1 1_c g_2\rangle + \left(\frac{\cos(\sqrt{2}gt)-1}{2}\right)|g_1 0_c e_2\rangle\Bigg]. \tag{34}$$

We observe that the time for complete state transfer, $t_f = \pi/\sqrt{2}g$, is the same as that for the polarized case.

B. Dispersive regime

Here, with the cavity dropping out of the subspace, the extended subspace accommodating the superposition state becomes the space spanned by the three-ket set $\{|e_1 g_2\rangle, |g_1 e_2\rangle, |g_1 g_2\rangle\}$. The evolution under the Tavis-Cummings Hamiltonian gives the time dependent state:

$$|\Psi(t)\rangle = \alpha|g_1 g_2\rangle + \beta\left(\tfrac{1}{2}\left(1+e^{-2ig^2t/\Delta}\right)|e_1 g_2\rangle + \tfrac{1}{2}\left(-1+e^{-2ig^2t/\Delta}\right)|g_1 e_2\rangle\right). \tag{35}$$

We observe that the time for complete state transfer, $t_f' = \pi\Delta/2g^2$, is the same as that for the polarized state.

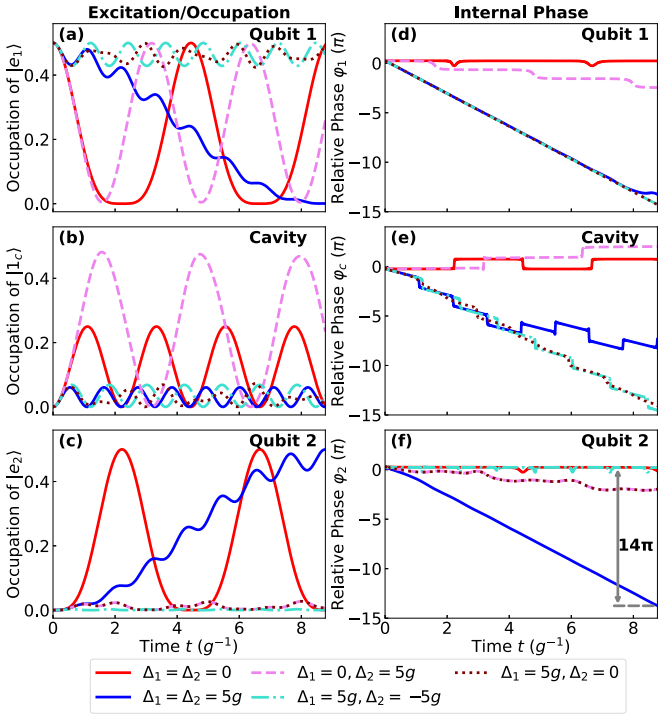


FIG. 9. For Qubit 1 initially in the equal superposition state, evolution of the excited state occupation of the qubits and the cavity [panels (a) through (c)], and their respective relative phases between the ground and the excited state [panels (d) through (f)], as a function of time. The system is tracked up to time $t_f'(\Delta = 5g)$ corresponding to the optimal transfer time in the dispersive regime. Phase data has been shifted to the cavity frame for illustration. The phase grows with a negative amplitude due to the mapping $\sigma_i^z = -Z_i$ as discussed in Sec. III.

C. General solution

In what follows, we use our quantum circuit to solve the problem for different combinations of detunings between the qubits and the cavity and we analyze both the short and the long-time dynamics.

1. Short time dynamics

We track the dynamics of the system up to a time corresponding to the complete state transfer (t_f) when the system is in a configuration with both qubits resonant with cavity. The simulation for this configuration agrees with the analytical expression in Eq. (34). Complete transfer of the superposition state from Qubit 1 to Qubit 2, with the relative phase shifted by π, occurs at a time t_f. This phase shift is immediately observed at $t > 0$, and is unperturbed for the duration of evolution.

2. Long time dynamics

Here, we explore the possibility of a slow but complete state transfer process by studying the long time dynamics of the system. This is presented in Fig. 9 where we show both the excited state occupation and the relative phase of Qubit 1, the cavity, and Qubit 2. Effective preservation (π shifted) of the relative phase is seen in the case of qubits

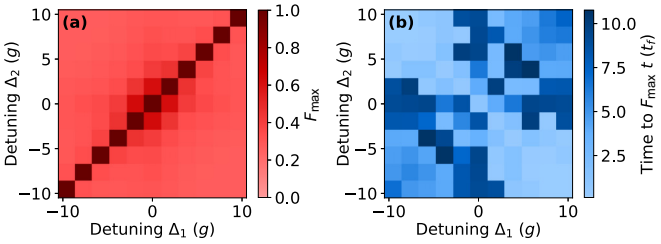


FIG. 10. (a) Heat map of the maximum achieved state transfer fidelity $F_{\max}$ as a function of detuning configurations. (b) Heat map of the time to achieve $F_{\max}$ as a function of detuning configurations.

resonant with the cavity, and also in the equally detuned configuration. In the latter case, the relative phase in Qubit 2 appears to drift far away, but it is important to note that it has been unwrapped (along 2π cycles) for better plot readability. So, the relative phase drift, which is exactly 14π (or seven 2π cycles), is preserved.

D. Fidelity

We also analyze the fidelity of the state transfer operation in the case of this equal superposition state. As in the previous case, we compute the fidelity as a function of the detunings between the qubits and the cavity by evolving the system up to a long time and identifying the maximal fidelity achieved. We also record our time to achieve this maximum fidelity. The results are shown in Figs. 10 (a) and 10(b). We note that the resonant and symmetrically detuned configurations ($\Delta_1 = \Delta_2$) form the diagonal and show complete state transfer, through the different mechanisms discussed above. Maximum fidelity rapidly drops with increasing detuning asymmetry. However, the smallest $F_{\max}$ is higher than that of the transfer of the fully polarized state, an effect that is due to the presence of the passive ground state component $|g_1 0_c g_2\rangle$, which is preserved in the evolution (within the regime of validity of the RWA, as discussed in Sec. VII). Just as in polarized state transfer, the resonant configuration achieves maximal fidelity early (at t_f) while the dispersive configurations ($\Delta_1 = \Delta_2 \gtrsim 5g$) achieve maximal fidelity over longer times (at $t_f'(\Delta)$), and the intermediate configurations ($g < \Delta_1 = \Delta_2 < 5g$) achieve maximal fidelity over much longer times. Note the subtle asymmetry in darkness along the diagonal, between positive and negative equal detuning configurations (a non-RWA effect).

VII. THE ROTATING WAVE APPROXIMATION

The RWA is often performed in the analytical solution or in the numerical simulation of the two-qubit quantum Rabi and parent Hamiltonians. It neglects the fast rotating terms in the interaction part of the Hamiltonian based on the following conditions:

$$\Delta_i \ll \omega_c + \omega_i, \tag{36}$$

$$g_i \ll \omega_c + \omega_i. \tag{37}$$

The resulting Hamiltonian is the Tavis-Cummings Hamiltonian [Eq. (15)]. When this Hamiltonian is mapped onto qubits,

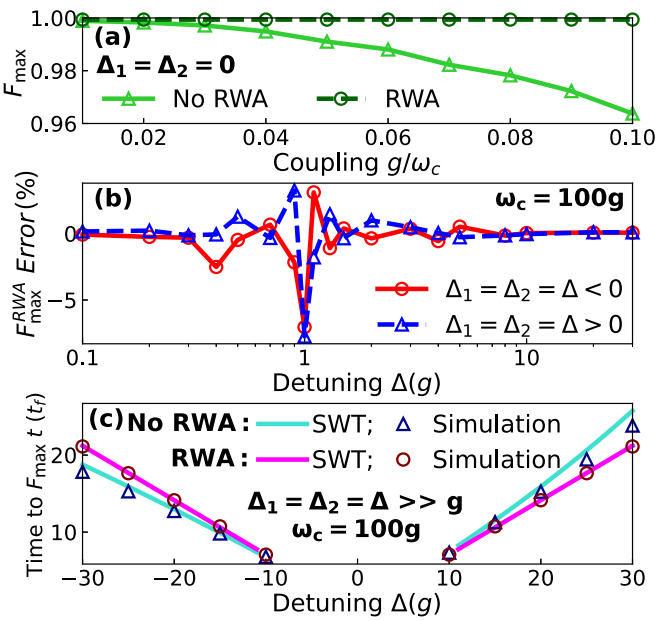


FIG. 11. (a) Maximum achieved fidelity for the full Hamiltonian (no RWA) and the RWA Hamiltonian. (b) Error in maximum fidelity due to the RWA as a function of detunings in the case of $\Delta_1 = \Delta_2 = \Delta$ for Δ positive (blue) and Δ negative (red). (c) Comparison of the time to maximum fidelity obtained through the quantum simulation with and without the rotating wave approximation vs the SWT result as a function of the detuning.

with $\hbar = 1$, we obtain the "qubitized" RWA Hamiltonian (see Appendix B):

$$H_q^{\mathrm{RWA}} = -\frac{\omega_1}{2}Z_1 - \frac{\omega_2}{2}Z_2 + \frac{\omega_c}{2}(I_c - Z_c) + \frac{g_1}{2}(X_c X_1 + Y_c Y_1) + \frac{g_2}{2}(X_c X_2 + Y_c Y_2). \tag{38}$$

To characterize the effect of the rotating wave approximation, we consider the full Hamiltonian in the frame rotating at the cavity frequency for the case where $g_1 = g_2 = g$ (see Appendix E):

$$H_{\mathrm{cavity}} = \frac{\Delta_1}{2}\sigma_1^z + \frac{\Delta_2}{2}\sigma_2^z + g(a_c^\dagger \sigma_1^- + a_c \sigma_1^+) + g(a_c^\dagger \sigma_2^- + a_c \sigma_2^+) + g e^{2i\omega_c t}(a_c^\dagger \sigma_1^+ + a_c^\dagger \sigma_2^+) + g e^{-2i\omega_c t}(a_c \sigma_1^- + a_c \sigma_2^-). \tag{39}$$

We note that the energy nonconserving terms (fifth and sixth terms) in Eq. (39) are fast oscillating and will average out over timescales corresponding to Δ or g if the conditions in Eqs. (36) and (37) are met. We simulate both Hamiltonians using our quantum circuit approach, with the cavity modeled to accommodate up to three excitations (see Appendix H) so that it can account for the effects of the energy nonconserving terms as shown in Appendix I. Figure 11 illustrates our comparison of the results from the full Hamiltonian against that of the RWA Hamiltonian when both Hamiltonians are simulated with the quantum algorithms. Figure 11(a) compares the maximum achieved fidelities as a function of the cavity-qubit coupling strength for qubits resonant with the cavity. As the coupling strength increases, we note a deviation between the

RWA and the full Hamiltonian result, as could be anticipated from the validity conditions of the RWA in Eqs. (36) and (37). Figure 11(b) shows the error in the maximum fidelity due to the RWA as a function of the detuning in the case of $\Delta_1 = \Delta_2 = \Delta$ for Δ positive (blue) and Δ negative (red). The error in maximum fidelity obtained from the RWA simulation is pronounced when $\Delta \sim g$, and shows an asymmetry with respect to Δ positive and Δ negative. Figure 11(c) shows a comparison of the time to maximum fidelity obtained through the quantum simulation with and without RWA, alongside the analytical result using the Schrieffer-Wolff transformation in both cases as a function of the detuning. It clearly indicates an asymmetry in the behaviors for Δ positive and for Δ negative. This asymmetry is clearly captured by the quantum simulation across the full range of the detuning values. To understand its origin, consider the dispersive regime. Here, upon performing the Schrieffer-Wolff transformation, an effective Hamiltonian derived for the full Hamiltonian in Eq. (1) can be obtained [56]. In this effective Hamiltonian, the effective interaction between the qubits acquires a correction that is indeed sensitive to the sign of detunings:

$$J = g_1 g_2 \left(\frac{1}{\Delta_1} + \frac{1}{\Delta_2} - \frac{1}{2\omega_1 - \Delta_1} - \frac{1}{2\omega_2 - \Delta_2} \right). \quad (40)$$

In agreement with the quantum circuits, this results in an asymmetry of the dynamics between the $\Delta_1 = \Delta_2 = \Delta > 0$ case and the $\Delta_1 = \Delta_2 = \Delta < 0$ case. This is manifested in the measured time to achieve the first complete state transfer, which for equal detunings is

$$t_f'' = \frac{\pi}{g^2\left(\frac{2}{\Delta} - \frac{2}{2\omega_1 - \Delta}\right)}. \quad (41)$$

VIII. CONCLUSION

We have implemented quantum circuits, that are compatible with NISQ-era systems, to study the efficiency of quantum state transfer between two qubits placed in a cavity as a function of various system parameters. The quantum algorithm solves the two-qubit quantum Rabi model describing the dynamics of the system, and allows us to reliably bypass conventional approximations that often inhibit analytical/numerical solutions, and to assess their regimes of validity. We are able to access the dispersive regime without resorting to a perturbative treatment such as the Schrieffer-Wolff transformation. We also solve the original Hamiltonian without performing the rotating wave approximation. Our approach allows us to map out the fidelity of the operation between the two qubits, and its dependence on various system parameters such as the emission frequencies of the qubits and the cavity frequency, as well as the respective qubit couplings to the cavity, and the damping factor of the cavity. Our quantum algorithm allows us to identify underexplored regimes of optimal performance such as the high-fidelity transfer in the intermediate detuning regime, and the efficient coupling of moderately detuned qubits by coupling them unequally to a far-detuned cavity. We examine the effect of the rotating wave approximation on the state transfer operation. The robustness of the present solution offers a promising avenue for simulating and optimizing photon-mediated operations in quantum information processing beyond the cavity-mediated two-qubit gates examined in this paper.

ACKNOWLEDGMENTS

We acknowledge support from the National Science Foundation under Grants No. PHY-2014023 and No. QIS-2328752. This work was also partially supported by AFRL/RI under Contract No. SA10032025060975. We thank W. A. Coish, V. V. Dobrovitski, and T. Thomay for useful discussions.

DATA AVAILABILITY

The data that support the findings of this article are not publicly available upon publication because it is not technically feasible and/or the cost of preparing, depositing, and hosting the data would be prohibitive within the terms of this research project. The data are available from the authors upon reasonable request.

APPENDIX A: MAPPING QUBIT AND CAVITY OPERATORS TO SPIN 1/2 OPERATORS IN THE SINGLE EXCITATION SUBSPACE

Qubits live in the two-dimensional state space of the spin 1/2 matrices. However, formally mapping them to the computational basis $\{|0\rangle, |1\rangle\}$ needs to account for any basis convention differences between the system and the algorithm. In the computational basis, the ground and excited states are defined as

$$|g\rangle \equiv |0\rangle \equiv \begin{bmatrix} 1 \\ 0 \end{bmatrix}, \quad |e\rangle \equiv |1\rangle \equiv \begin{bmatrix} 0 \\ 1 \end{bmatrix}. \quad (A1)$$

The Pauli matrices corresponding to this basis are

$$\begin{aligned} X &= |e\rangle\langle g| + |g\rangle\langle e|, \\ Y &= i|e\rangle\langle g| - i|g\rangle\langle e|, \\ Z &= |g\rangle\langle g| - |e\rangle\langle e| \end{aligned} \quad (A2)$$

Our two-qubit extension of the quantum Rabi system is defined in the convention generally used in quantum optics, where the definition of $|0\rangle$ and $|1\rangle$ are flipped relative to that in the computational basis. This leads to the requirement of a formal mapping of our system's operators to the computational Pauli matrices, which we perform below [46].

$$\sigma^z = |e\rangle\langle e| - |g\rangle\langle g| = -Z, \quad (A3)$$

$$\sigma^+ = |e\rangle\langle g| = \tfrac{1}{2}(X - iY), \quad (A4)$$

$$\sigma^- = |g\rangle\langle e| = \tfrac{1}{2}(X + iY). \quad (A5)$$

The bosonic cavity operators are defined as

$$a = \sum_{n=1}^{\infty} \sqrt{n}|n-1\rangle\langle n|, \quad (A6)$$

$$a^\dagger = \sum_{n=0}^{\infty} \sqrt{n+1}|n+1\rangle\langle n|. \quad (A7)$$

We map a and $a^\dagger$ to the computational Pauli matrices by representing the cavity as a qubit. This mapping is enabled by

constraining the total excitation in the system to remain equal to 1, which is reasonable when the system is initially prepared with just one excitation, is isolated, and is operated away from the ultrastrong or deep-dispersive regimes, as discussed in the introduction and justified in Appendix I. This restricts our state space to the single excitation subspace, where $n \in \{0, 1\}$. The cavity can then be treated as a qubit, and its operators defined above can be mapped to the computational Pauli matrices as

$$a = |0\rangle\langle 1| = \sigma^- = \tfrac{1}{2}(X + \mathrm{i}Y), \tag{A8}$$

$$a^\dagger = |1\rangle\langle 0| = \sigma^+ = \tfrac{1}{2}(X - \mathrm{i}Y). \tag{A9}$$

APPENDIX B: QUBITIZATION OF THE TWO-QUBIT QUANTUM RABI HAMILTONIAN

Here, we "qubitize" the two-qubit quantum Rabi Hamiltonian in Eq. (1) using the operator transformations in Eq. (3). We first transform the interactions terms as follows:

$$\begin{aligned} a_c^\dagger \sigma_i^- &= \tfrac{1}{2}(X_c - \mathrm{i}Y_c)\tfrac{1}{2}(X_i + \mathrm{i}Y_i) \\ &= \tfrac{1}{4}(X_cX_i + \mathrm{i}X_cY_i - \mathrm{i}Y_cX_i + Y_cY_i), \end{aligned} \tag{B1}$$

$$\begin{aligned} a_c \sigma_i^+ &= \tfrac{1}{2}(X_c + \mathrm{i}Y_c)\tfrac{1}{2}(X_i - \mathrm{i}Y_i) \\ &= \tfrac{1}{4}(X_cX_i - \mathrm{i}X_cY_i + \mathrm{i}Y_cX_i + Y_cY_i), \end{aligned} \tag{B2}$$

$$\begin{aligned} a_c^\dagger \sigma_i^+ &= \tfrac{1}{2}(X_c - \mathrm{i}Y_c)\tfrac{1}{2}(X_i - \mathrm{i}Y_i) \\ &= \tfrac{1}{4}(X_cX_i - \mathrm{i}X_cY_i - \mathrm{i}Y_cX_i - Y_cY_i), \end{aligned} \tag{B3}$$

$$\begin{aligned} a_c \sigma_i^- &= \tfrac{1}{2}(X_c + \mathrm{i}Y_c)\tfrac{1}{2}(X_i + \mathrm{i}Y_i) \\ &= \tfrac{1}{4}(X_cX_i + \mathrm{i}X_cY_i + \mathrm{i}Y_cX_i - Y_cY_i). \end{aligned} \tag{B4}$$

It is easy to see that all but the X_cX_i terms cancel out in the above transformations, leading to a concise "qubitized" Hamiltonian, given by

$$H_q = -\frac{\omega_1}{2}Z_1 - \frac{\omega_2}{2}Z_2 + \frac{\omega_c}{2}(I_c - Z_c) + g_1(X_cX_1) + g_2(X_cX_2). \tag{B5}$$

When the rotating wave approximation is applied, we drop the energy nonconserving terms [Eqs. (B3) and (B4)] and obtain the "qubitized" Hamiltonian in the RWA as follows:

$$\begin{aligned} H_q^{\mathrm{RWA}} &= -\frac{\omega_1}{2}Z_1 - \frac{\omega_2}{2}Z_2 + \frac{\omega_c}{2}(I_c - Z_c) \\ &\quad + \frac{g_1}{2}(X_cX_1 + Y_cY_1) + \frac{g_2}{2}(X_cX_2 + Y_cY_2). \end{aligned} \tag{B6}$$

APPENDIX C: EXACT SOLUTION TO THE TAVIS-CUMMINGS HAMILTONIAN WHEN THE QUBITS ARE RESONANT WITH THE CAVITY

In this appendix, we derive $\Psi(t)$ for the special case where the qubits are resonant with the cavity, and with an initial state of the system where Qubit 1 is in a superposition state, and the cavity and Qubit 2 are empty and in the ground state, respectively.

$$|\Psi(0)\rangle = \alpha|g_1 0_c g_2\rangle + \beta|e_1 0_c g_2\rangle. \tag{C1}$$

The Tavis-Cummings Hamiltonian then becomes

$$H = g_1(a_c^\dagger \sigma_1^- + a_c \sigma_1^+) + g_2(a_c^\dagger \sigma_2^- + a_c \sigma_2^+). \tag{C2}$$

Since we are interested in the time evolution of a superposition state, we consider the extended single excitation subspace accommodating the ground state component, given by

$$\mathcal{H}_{\mathrm{reduced}} = \{|e_1 0_c g_2\rangle, |g_1 1_c g_2\rangle, |g_1 0_c e_2\rangle, |g_1 0_c g_2\rangle\}. \tag{C3}$$

In the subspace ordered as such, the matrix representation of the Hamiltonian is

$$H = \begin{bmatrix} 0 & g_1 & 0 & 0 \\ g_1 & 0 & g_2 & 0 \\ 0 & g_2 & 0 & 0 \\ 0 & 0 & 0 & 0 \end{bmatrix}. \tag{C4}$$

We note that the state $|g_1 0_c g_2\rangle$ is not affected by the Hamiltonian's dynamics and is therefore preserved during the time evolution of the system. This, along with the linearity of the evolution operator $U(t)$, enables us to write

$$|\Psi(t)\rangle = \alpha|\Psi_g(t)\rangle + \beta|\Psi_e(t)\rangle \tag{C5}$$

$$= \alpha|\Psi_g(0)\rangle + \beta(U(t)|\Psi_e(0)\rangle) \tag{C6}$$

$$= \alpha|g_1 0_c g_2\rangle + \beta(U(t)|e_1 0_c g_2\rangle). \tag{C7}$$

We solve for $\Psi_e(t)$ using the method of exact diagonalization in the single excitation subspace $\{|e_1 0_c g_2\rangle, |g_1 1_c g_2\rangle, |g_1 0_c e_2\rangle\}$. In this basis, the Hamiltonian in the matrix representation becomes

$$H = \begin{bmatrix} 0 & g_1 & 0 \\ g_1 & 0 & g_2 \\ 0 & g_2 & 0 \end{bmatrix}. \tag{C8}$$

The eigenvalues and eigenvectors of H are

$$E_1 = 0. \tag{C9}$$

$$E_2 = \sqrt{g_1^2 + g_2^2}, \tag{C10}$$

$$E_3 = -\sqrt{g_1^2 + g_2^2}, \tag{C11}$$

$$|E_1\rangle = \frac{g_2}{\sqrt{g_1^2 + g_2^2}}|e_1 0_c g_2\rangle - \frac{g_1}{\sqrt{g_1^2 + g_2^2}}|g_1 0_c e_2\rangle, \tag{C12}$$

$$\begin{aligned} |E_2\rangle &= \frac{1}{\sqrt{2(g_1^2 + g_2^2)}}(g_1|e_1 0_c g_2\rangle + g_2|g_1 0_c e_2\rangle) \\ &\quad + \frac{1}{\sqrt{2}}|g_1 1_c g_2\rangle, \end{aligned} \tag{C13}$$

$$\begin{aligned} |E_3\rangle &= \frac{1}{\sqrt{2(g_1^2 + g_2^2)}}(g_1|e_1 0_c g_2\rangle + g_2|g_1 0_c e_2\rangle) \\ &\quad - \frac{1}{\sqrt{2}}|g_1 1_c g_2\rangle. \end{aligned} \tag{C14}$$

$|e_1 0_c g_2\rangle$ can be represented in the energy eigenbasis $\{|E_i\rangle\}$ as

$$|e_1 0_c g_2\rangle = \frac{g_2}{\sqrt{g_1^2+g_2^2}}|E_1\rangle + \frac{g_1}{\sqrt{2\left(g_1^2+g_2^2\right)}}(|E_2\rangle + |E_3\rangle). \tag{C15}$$

The evolution operator $U(t) = e^{-iHt}$ acts trivially in this representation:

$$|\Psi_e(t)\rangle = U(t)\left(\frac{g_2}{\sqrt{g_1^2+g_2^2}}|E_1\rangle + \frac{g_1}{\sqrt{2\left(g_1^2+g_2^2\right)}}(|E_2\rangle + |E_3\rangle)\right), \tag{C16}$$

$$= \frac{g_2}{\sqrt{g_1^2+g_2^2}}|E_1\rangle + \frac{g_1}{\sqrt{2\left(g_1^2+g_2^2\right)}}\left(e^{-i\sqrt{g_1^2+g_2^2}t}|E_2\rangle + e^{i\sqrt{g_1^2+g_2^2}t}|E_3\rangle\right). \tag{C17}$$

Reexpressing in the original basis and grouping by basis states, we get

$$|\Psi_e(t)\rangle = \left(\frac{g_2^2}{g_1^2+g_2^2} + \frac{\left(e^{-i\sqrt{g_1^2+g_2^2}t} + e^{i\sqrt{g_1^2+g_2^2}t}\right)g_1^2}{2\left(g_1^2+g_2^2\right)}\right)|e_1 0_c g_2\rangle + \left(\frac{\left(e^{-i\sqrt{g_1^2+g_2^2}t} - e^{i\sqrt{g_1^2+g_2^2}t}\right)g_1}{2\sqrt{g_1^2+g_2^2}}\right)|g_1 1_c g_2\rangle$$
$$+\left(\frac{-g_1 g_2}{g_1^2+g_2^2} + \frac{\left(e^{-i\sqrt{g_1^2+g_2^2}t} + e^{i\sqrt{g_1^2+g_2^2}t}\right)g_1 g_2}{2\left(g_1^2+g_2^2\right)}\right)|g_1 0_c e_2\rangle, \tag{C18}$$

$$|\Psi_e(t)\rangle = \frac{g_1^2\cos\left(\sqrt{g_1^2+g_2^2}t\right)+g_2^2}{g_1^2+g_2^2}|e_1 0_c g_2\rangle - \frac{ig_1\sin\left(\sqrt{g_1^2+g_2^2}t\right)}{\sqrt{g_1^2+g_2^2}}|g_1 1_c g_2\rangle + \frac{g_1 g_2\left(\cos\left(\sqrt{g_1^2+g_2^2}t\right)-1\right)}{g_1^2+g_2^2}|g_1 0_c e_2\rangle. \tag{C19}$$

Plugging this into Eq. (C7), we get the exact solution for a superposition state as

$$|\Psi(t)\rangle = \alpha|g_1 0_c g_2\rangle + \beta\left[\frac{g_1^2\cos\left(\sqrt{g_1^2+g_2^2}t\right)+g_2^2}{g_1^2+g_2^2}|e_1 0_c g_2\rangle - \frac{ig_1\sin\left(\sqrt{g_1^2+g_2^2}t\right)}{\sqrt{g_1^2+g_2^2}}|g_1 1_c g_2\rangle\right.$$
$$\left.+\frac{g_1 g_2\left(\cos\left(\sqrt{g_1^2+g_2^2}t\right)-1\right)}{g_1^2+g_2^2}|g_1 0_c e_2\rangle\right]. \tag{C20}$$

For $g_1 = g_2$, we get

$$|\Psi(t)\rangle = \alpha|g_1 0_c g_2\rangle + \beta\left[\frac{1+\cos(\sqrt{2}gt)}{2}|e_1 0_c g_2\rangle - \frac{i\sin(\sqrt{2}gt)}{\sqrt{2}}|g_1 1_c g_2\rangle + \frac{\cos(\sqrt{2}gt)-1}{2}|g_1 0_c e_2\rangle\right]. \tag{C21}$$

At $t = 0$, we recover the initial state

$$|\Psi(0)\rangle = \alpha|g_1 0_c g_2\rangle + \beta|e_1 0_c g_2\rangle. \tag{C22}$$

At $t = \frac{t_f}{2} = \frac{\pi}{2\sqrt{2}g}$, the cavity reaches its maximum occupation, which is equal to half the total excitation:

$$\left|\Psi\left(\frac{\pi}{2\sqrt{2}g}\right)\right\rangle = \alpha|g_1 0_c g_2\rangle + \beta\left(\frac{1}{2}|e_1 0_c g_2\rangle - \frac{i}{\sqrt{2}}|g_1 1_c g_2\rangle - \frac{1}{2}|g_1 0_c e_2\rangle\right). \tag{C23}$$

At $t = t_f = \frac{\pi}{\sqrt{2}g}$, there is complete state transfer from Qubit 1 to Qubit 2, with the relative phase shifted by π:

$$\left|\Psi\left(\frac{\pi}{\sqrt{2}g}\right)\right\rangle = \alpha|g_1 0_c g_2\rangle - \beta|g_1 0_c e_2\rangle. \tag{C24}$$

This phase shift can be corrected using a Z gate.

APPENDIX D: EXACT SOLUTION FOR THE TIME-DEPENDENT FIDELITY IN THE INTERMEDIATE DETUNING REGIME

To simplify the algebra, we adopt the basis set $\{|B\rangle, |g_1 1_c g_2\rangle, |D\rangle\}$, where $|B\rangle$ and $|D\rangle$ are bright and dark states respectively, and are defined as

$$|B\rangle = \frac{1}{\sqrt{2}}(|e_1 0_c g_2\rangle + |g_1 0_c e_2\rangle), \tag{D1}$$

$$|D\rangle = \frac{1}{\sqrt{2}}(|e_1 0_c g_2\rangle - |g_1 0_c e_2\rangle). \tag{D2}$$

The initial and target states of the system in this basis are

$$|\Psi(0)\rangle = |e_1 0_c g_2\rangle = \frac{1}{\sqrt{2}}(|B\rangle + |D\rangle), \tag{D3}$$

$$|\Psi_{\text{target}}\rangle = |g_1 0_c e_2\rangle = \frac{1}{\sqrt{2}}(|B\rangle - |D\rangle). \tag{D4}$$

The fidelity of the time dependent state of the system with respect to the target state is

$$\begin{aligned} F(t) &= |\langle\Psi_{\text{target}}|\Psi(t)\rangle|^2 \\ &= \tfrac{1}{4}|(\langle B| - \langle D|)(|B(t)\rangle + |D(t)\rangle)|^2 \\ &= \tfrac{1}{4}|c_B(t) - 1|^2. \end{aligned} \tag{D5}$$

The problem reduces to finding $c_B(t)$. In the subspace $\{|B\rangle, |g_1 1_c g_2\rangle, |D\rangle\}$ ordered as such, the matrix representation of the Tavis-Cummings Hamiltonian in the cavity frame is

$$H = \begin{bmatrix} 0 & \sqrt{2}g & 0 \\ \sqrt{2}g & -\Delta & 0 \\ 0 & 0 & 0 \end{bmatrix}. \tag{D6}$$

The dark state $|D\rangle$ is decoupled, and thus the dynamics can be represented by a 2×2 matrix in the $\{|B\rangle, |g_1 1_c g_2\rangle\}$ basis:

$$H' = \begin{bmatrix} 0 & \sqrt{2}g \\ \sqrt{2}g & -\Delta \end{bmatrix}. \tag{D7}$$

The eigenvalues and eigenvectors of H' are

$$\begin{aligned} E_+ &= \frac{-\Delta}{2} + \frac{\Omega}{2}, \\ E_- &= \frac{-\Delta}{2} - \frac{\Omega}{2}, \\ |E_+\rangle &= |B\rangle + \frac{E_+}{\sqrt{2}g}|g_1 1_c g_2\rangle, \\ |E_-\rangle &= |B\rangle + \frac{E_-}{\sqrt{2}g}|g_1 1_c g_2\rangle. \end{aligned} \tag{D8}$$

The bright state $|B\rangle$ can be represented in the eigenbasis of H' and its evolution $|B(t)\rangle$ can be calculated in it:

$$|B\rangle = \frac{E_-}{E_- - E_+}|E_+\rangle - \frac{E_+}{E_- - E_+}|E_-\rangle, \tag{D9}$$

$$\begin{aligned} |B(t)\rangle &= e^{-iH't}|B\rangle \\ &= -\frac{E_-}{\Omega}e^{-iE_+t}|E_+\rangle + \frac{E_+}{\Omega}e^{-iE_-t}|E_-\rangle. \end{aligned} \tag{D10}$$

From this, we can get

$$c_B(t) = \langle B|B(t)\rangle \tag{D11}$$

$$= -\frac{E_-}{\Omega}e^{-iE_+t} + \frac{E_+}{\Omega}e^{-iE_-t}. \tag{D12}$$

Plugging this into Eq. (D5),

$$\begin{aligned} F(t) = \frac{1}{4}\Bigg[1 + \frac{E_+^2}{\Omega^2} + \frac{E_-^2}{\Omega^2} - 2E_+E_-\cos(\Omega t) \\ + 2\frac{E_-}{\Omega}\cos(E_+t) - 2\frac{E_+}{\Omega}\cos(E_-t)\Bigg]. \end{aligned} \tag{D13}$$

Substituting for E_+ and E_- from Eq. (D8) and simplifying, we get

$$\begin{aligned} F(t) = \frac{1}{4}\Bigg[1 + \frac{1}{2}\left(1 + \frac{\Delta^2}{\Omega^2}\right) + \frac{1}{2}\left(1 - \frac{\Delta^2}{\Omega^2}\right)\cos(\Omega t) \\ - 2\cos\left(\frac{\Delta}{2}t\right)\cos\left(\frac{\Omega}{2}t\right) \\ - \frac{2\Delta}{\Omega}\sin\left(\frac{\Delta}{2}t\right)\sin\left(\frac{\Omega}{2}t\right)\Bigg]. \end{aligned} \tag{D14}$$

APPENDIX E: THE TWO-QUBIT QUANTUM RABI HAMILTONIAN IN THE CAVITY FRAME

In order to express the Hamiltonian only in terms of the detunings Δ_i and the couplings g_i, we move H in Eq. (1) to the rotating frame of the cavity ω_c using a frame transformation:

$$H_{\text{cavity}} = UHU^\dagger - iU\frac{\partial U^\dagger}{\partial t}, \tag{E1}$$

where $U(t) = e^{iGt}$ is the frame rotation operator based on the generator:

$$G = \omega_c\left(\frac{\sigma_1^z}{2} + \frac{\sigma_2^z}{2} + a_c^\dagger a_c\right). \tag{E2}$$

Since G is time independent, Eq. (E1) reduces to

$$\begin{aligned} H_{\text{cavity}} &= UHU^\dagger - iU(-iG)U^\dagger \\ &= UHU^\dagger - G \\ &= UHU^\dagger - \omega_c\left(\frac{\sigma_1^z}{2} + \frac{\sigma_2^z}{2} + a_c^\dagger a_c\right). \end{aligned} \tag{E3}$$

Using the relation $e^{i\theta G}Ae^{-i\theta G} = e^{-i\theta\lambda}A$ when $[G, A] = -\lambda A$, we get

$$\begin{aligned} U\sigma_i^z U^\dagger &= \sigma_i^z, \\ U\sigma_i^+ U^\dagger &= e^{i\omega_c t}\sigma_i^+, \\ U\sigma_i^- U^\dagger &= e^{-i\omega_c t}\sigma_i^-, \\ Ua_c^\dagger U^\dagger &= e^{i\omega_c t}a_c^\dagger, \\ Ua_c U^\dagger &= e^{-i\omega_c t}a_c. \end{aligned} \tag{E4}$$

Plugging the operator transformations from Eq. (E4) into the Hamiltonian transformation in Eq. (E3), we get the two-qubit quantum Rabi Hamiltonian in the rotating frame of the cavity, with $\hbar = 1$ as follows:

$$\begin{aligned} H_{\text{cavity}} = \frac{\Delta_1}{2}\sigma_1^z + \frac{\Delta_2}{2}\sigma_2^z + g_1(a_c^\dagger\sigma_1^- + a_c\sigma_1^+) \\ + g_2(a_c^\dagger\sigma_2^- + a_c\sigma_2^+) + e^{2i\omega_c t}(g_1 a_c^\dagger\sigma_1^+ + g_2 a_c^\dagger\sigma_2^+) \\ + e^{-2i\omega_c t}(g_1 a_c\sigma_1^- + g_2 a_c\sigma_2^-). \end{aligned} \tag{E5}$$

We note that rotation to the cavity frame introduces fast oscillations to the couplings of the energy nonconserving terms.

APPENDIX F: ESTIMATING THE SYSTEMATIC ERROR IN THE SIMULATION OF THE "QUBITIZED" HAMILTONIAN USING THE CAVITY FRAME

The systematic Trotter error is typically associated with the timescales (inverse frequencies) involved in the system. However, there is a risk of overestimating this error if we do not recognize the relative dynamics in the system. In our two-qubit quantum Rabi Hamiltonian, we note that the relative dynamics are of the order g, Δ, which can be seen by transforming the Hamiltonian to the cavity frame as H_{cavity} [Eq. (E5)]. We proceed to "qubitize" H_{cavity} using the relations in Eq. (3) and get

$$\begin{aligned}
H^q_{\text{cavity}} &= \sum_{i=1,2} -\frac{\Delta_i}{2}Z_i + \frac{g_i}{2}(X_cX_i + Y_cY_i) \\
&\quad + \frac{g_i}{4}e^{2i\omega_c t}(X_cX_i - Y_cY_i - iX_cY_i - iY_cX_i) \\
&\quad + \frac{g_i}{4}e^{-2i\omega_c t}(X_cX_i - Y_cY_i + iX_cY_i + iY_cX_i), \\
&= \sum_{i=1,2} -\frac{\Delta_i}{2}Z_i + \frac{g_i}{2}(X_cX_i + Y_cY_i) \\
&\quad + \frac{g_i}{4}(e^{2i\omega_c t} + e^{-2i\omega_c t})(X_cX_i - Y_cY_i) \\
&\quad - i\frac{g_i}{4}(e^{2i\omega_c t} - e^{-2i\omega_c t})(X_cY_i + iY_cX_i) \\
&= \sum_{i=1,2} -\frac{\Delta_i}{2}Z_i + \frac{g_i}{2}(X_cX_i + Y_cY_i) \\
&\quad + \frac{g_i}{2}\cos(2\omega_c t)(X_cX_i - Y_cY_i) \\
&\quad + \frac{g_i}{2}\sin(2\omega_c t)(X_cY_i + iY_cX_i). \qquad \text{(F1)}
\end{aligned}$$

We note that H^q_{cavity} has the structure $H^0_i + H_{ci}$, where H^0_i is the free evolution of the ith qubit and H_{ci} is the interaction of the cavity with the ith qubit. We leverage this structure to split the Hamiltonian as follows:

$$H^q_{\text{cavity}} = H^0 + H_{c1} + H_{c2}, \qquad \text{(F2)}$$

where $H^0 = H^0_1 + H^0_2$. The first-order Trotter error per step, $\epsilon = ||e^{-iH\delta t} - U_T(\delta t)||$, is estimated as

$$\begin{aligned}
\epsilon &\sim \frac{\delta t^2}{2}([H^0, H_{1c}] + [H^0, H_{2c}] + [H_{1c}, H_{2c}]) \\
&\sim \delta t^2(g_1\Delta_1 + g_2\Delta_2 + g_1g_2). \qquad \text{(F3)}
\end{aligned}$$

The total error over a simulation time T, represented by $N = T/\delta t$ steps, accumulates at most linearly [57], and therefore has an upper bound given by

$$\epsilon_{\text{tot}} \sim (g_1\Delta_1 + g_2\Delta_2 + g_1g_2)T\delta t. \qquad \text{(F4)}$$

This conservative estimate serves to provide a reasonable reference time-step size for the corresponding simulation, which can be further optimized through empirical methods.

APPENDIX G: QUANTUM CIRCUIT FOR THE TWO-QUBIT QUANTUM RABI HAMILTONIAN WITH A DAMPED CAVITY

The time evolution of the density matrix only due to the dissipator in the master equation in Eq. (24) is given by

$$\begin{aligned}
\frac{d}{dt}\rho_c &= \mathcal{L}_D(\rho_c) \\
&= \kappa a\rho_c a^\dagger - \frac{\kappa}{2}\{a^\dagger a, \rho_c\} \\
&= \kappa a(\rho_{00}|0\rangle|\langle 0| + \rho_{01}|0\rangle|\langle 1| \\
&\quad + \rho_{10}|1\rangle|\langle 0| + \rho_{11}|1\rangle|\langle 1|)a^\dagger \\
&\quad - \frac{\kappa}{2}\{a^\dagger a, (\rho_{00}|0\rangle|\langle 0| + \rho_{01}|0\rangle|\langle 1| \\
&\quad + \rho_{10}|1\rangle|\langle 0| + \rho_{11}|1\rangle|\langle 1|)\} \\
&= \kappa\rho_{11}|0\rangle|\langle 0| - \frac{\kappa}{2}\rho_{01}|0\rangle|\langle 1| \\
&\quad - \frac{\kappa}{2}\rho_{10}|1\rangle|\langle 0| - \kappa\rho_{11}|1\rangle|\langle 1|. \qquad \text{(G1)}
\end{aligned}$$

From the above, we obtain the following differential equations for the density matrix elements ρ_{ij}:

$$\begin{aligned}
\frac{d}{dt}\rho_{00} &= \kappa\rho_{11}, \\
\frac{d}{dt}\rho_{01} &= -\frac{\kappa}{2}\rho_{01}, \\
\frac{d}{dt}\rho_{10} &= -\frac{\kappa}{2}\rho_{10}, \\
\frac{d}{dt}\rho_{11} &= -\kappa\rho_{11}. \qquad \text{(G2)}
\end{aligned}$$

Integrating these differential equations from t to $t + \delta t$, we get

$$\begin{aligned}
\rho_{00}(t+\delta t) &= \rho_{00}(t) + (1 - e^{-\kappa\delta t})\rho_{11}(t), \\
\rho_{01}(t+\delta t) &= e^{-\kappa\delta t/2}\rho_{01}(t), \\
\rho_{10}(t+\delta t) &= e^{-\kappa\delta t/2}\rho_{10}(t), \\
\rho_{11}(t+\delta t) &= e^{-\kappa\delta t}\rho_{11}(t).
\end{aligned}$$

The above transformations correspond to applying $e^{\mathcal{L}_D\delta t}$ on the cavity density matrix $\rho_c(t)$ and can also be exactly obtained using a Kraus map defined as

$$\mathcal{M}(\rho_c) = \Omega_0\rho_c\Omega_0^\dagger + \Omega_1\rho_c\Omega_1^\dagger, \qquad \text{(G3)}$$

where

$$\Omega_0 = |0\rangle\langle 0| + \sqrt{1-\gamma^2}|1\rangle\langle 1|, \qquad \text{(G4)}$$

$$\Omega_1 = \gamma|0\rangle\langle 1|, \qquad \text{(G5)}$$

and

$$\gamma = \sqrt{1 - e^{-\kappa\delta t}}. \qquad \text{(G6)}$$

The map $\mathcal{M}$ can be represented in a quantum circuit through an amplitude damping arrangement as shown by Gupta and Chandrashekar [54]. Figure 12 shows the quantum circuit that corresponds to the evolution of the quantum Rabi Hamiltonian with cavity damping as per the Lindblad master equation.

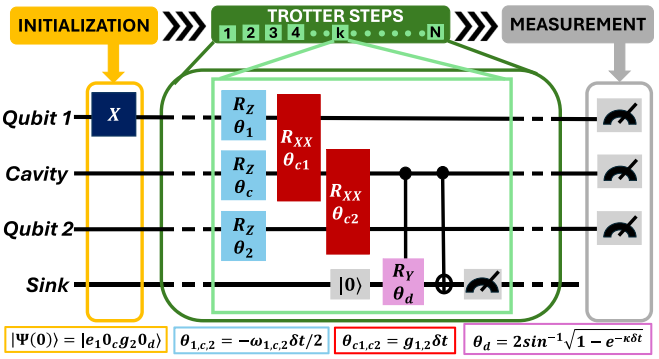


FIG. 12. Quantum circuit for simulating the two-qubit quantum Rabi Hamiltonian along with cavity damping. The arrangement involves a ancillary damping qubit called the sink, which draws population out of the cavity at a rate κ. The sink is reset to $|0\rangle$ before each Trotter step and measured after it, to ensure a "one-way" flow of excitation to it from the cavity.

APPENDIX H: QUBIT HAMILTONIAN FOR THE TWO-QUBIT QUANTUM RABI HAMILTONIAN WITH A FOUR-LEVEL CAVITY

We use binary encoding to represent higher cavity states using multiple qubits. A cavity with a cutoff $n_c^{\max} = 3$ can be represented using two qubits. The corresponding Hamiltonian is given by

$$\begin{aligned} H_q = &-\frac{\omega_1}{2}Z_1 - \frac{\omega_2}{2}Z_2 + \frac{\omega_c}{2}\left(\frac{3}{2}I_{c1}I_{c2} - Z_{c1}I_{c2} - \frac{1}{2}I_{c1}Z_{c2}\right) \\ &+ g_1\left(\frac{1+\sqrt{3}}{2}X_1 I_{c1}X_{c2} + \frac{1-\sqrt{3}}{2}X_1 Z_{c1}X_{c2}\right) \\ &+ \frac{1}{\sqrt{2}}X_1 X_{c1}X_{c2} + \frac{1}{\sqrt{2}}X_1 Y_{c1}Y_{c2}\Big) + g_2\Big(\frac{1+\sqrt{3}}{2}X_2 I_{c1}X_{c2} \\ &+ \frac{1-\sqrt{3}}{2}X_2 Z_{c1}X_{c2}) + \frac{1}{\sqrt{2}}X_2 X_{c1}X_{c2} + \frac{1}{\sqrt{2}}X_2 Y_{c1}Y_{c2}\Big). \end{aligned} \tag{H1}$$

APPENDIX I: PROBABILITY OF OCCUPATION OF HIGHER EXCITED STATES OF THE CAVITY AND ITS EFFECT ON STATE TRANSFER FIDELITY

For a closed system with a single excitation, the probability of occupation of cavity states higher than $|1_c\rangle$ is determined by the strength of energy nonconserving terms in the Hamiltonian in Eq. (1). In the regime where $g_i, \Delta_i \ll \omega_c + \omega_i$, this strength is weak and can be treated as a perturbation. As seen in Appendix J, such a treatment gives an estimate for the probability of occupation of a cavity level $|n_c\rangle$:

$$P_{\max}(|n_c\rangle) \sim \left(\frac{g}{\omega_c}\right)^{2\lfloor n/2 \rfloor}. \tag{I1}$$

The estimate above is validated through simulation results shown in Fig. 13. Panel (a) shows the maximum probability of occupation of the first four excited states of the cavity during resonant transfer of excitation between the qubits as a function of the coupling g/ω_c when the cavity can accommodate upto four excitations ($n_c^{\max} = 4$). The dashed lines represent the analytical estimate from Eq. (J9). The population in $n_c > 1$ becomes appreciable as we approach the ultrastrong coupling (USC) regime ($g/\omega_c > 0.01$). Even in the USC regime ($g/\omega_c = 0.01$), $n_c = 4$ is negligibly populated, which implies that the drop in fidelity as we approach USC, while understated by modeling the cavity with $n_c^{\max} = 1$, is sufficiently well captured with $n_c^{\max} = 3$. This is confirmed in panel (b), which shows the drop in fidelity as a function of the coupling g/ω_c for various cavity cutoffs $n_c^{\max}$, in which we see a negligible difference in fidelity between $n_c^{\max} = 3$ and $n_c^{\max} = 4$.

APPENDIX J: PROOF OF THE ESTIMATE FOR THE PROBABILITY OF CAVITY LEVEL OCCUPATION

To estimate the effect of the energy nonconserving terms in Eq. (1) toward populating higher cavity levels ($n_c > 1$), we move to the interaction frame of the Hamiltonian, and then treat the fast-oscillating energy nonconserving terms as

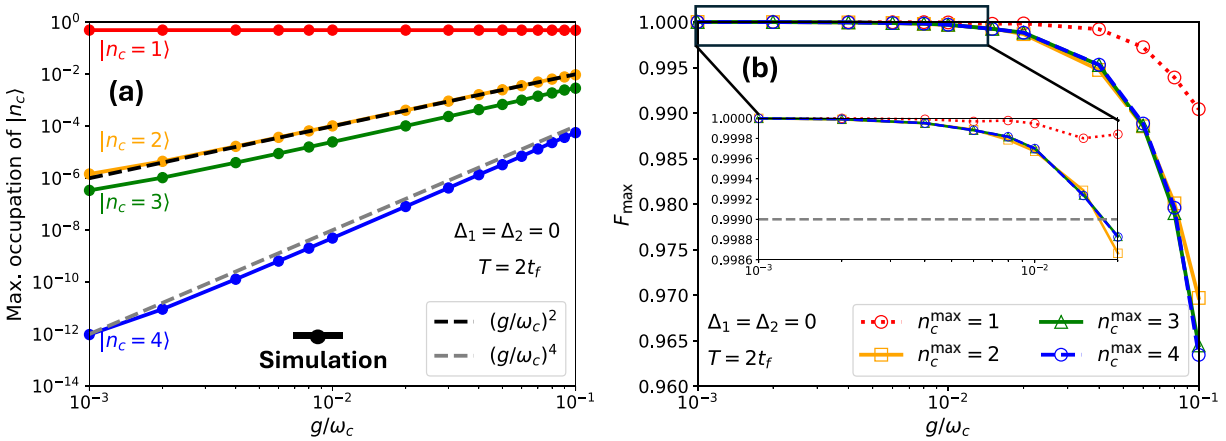


FIG. 13. Illustration of the effect of coupling g/ω_c on cavity level cutoff. (a) Maximum occupation of the first four excited states of the cavity during resonant transfer of the polarized state when the qubits are resonant with the cavity, as a function of the couplings g/ω_c. (b) Maximum fidelity during the resonant transfer of the polarized state as a function of the couplings g/ω_c, for different cavity cutoffs $n_c^{\max}$.

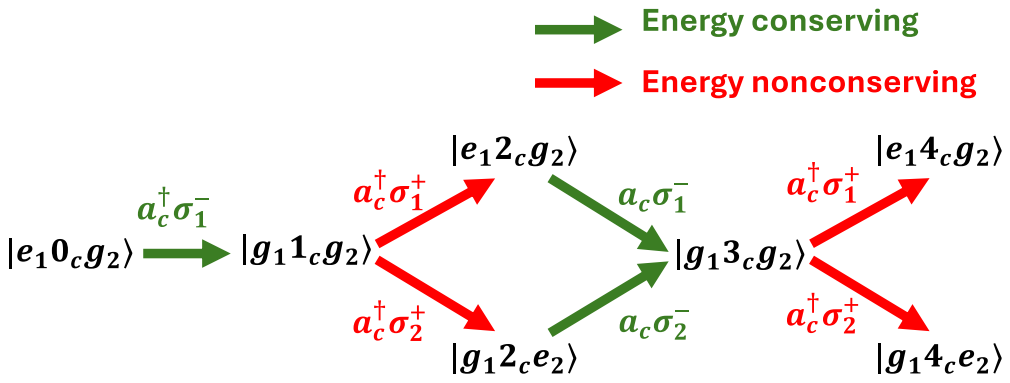


FIG. 14. A diagrammatic representation of the pathways representing the lowest order in the energy nonconserving terms (perturbation) required to populate up to the fourth excited state of the cavity.

a perturbation:

$$H_I(t) = \sum_{i=1}^{2} \hbar g_j \big(e^{-i\Delta_i t} a_c^\dagger \sigma_i^- + e^{i\Delta_i t} a_c \sigma_i^+ + e^{i(2\omega_c+\Delta_i)t} a_c^\dagger \sigma_i^+ + e^{-i(2\omega_c+\Delta_i)t} a_c \sigma_i^-\big). \quad \text{(J1)}$$

This can be organized as

$$H_I(t) = H_I^{(0)}(t) + V_I(t), \quad \text{(J2)}$$

with

$$V_I(t) = \sum_{i=1}^{2} \hbar g_i \big(e^{i(2\omega_c+\Delta_i)t} a_c^\dagger \sigma_i^+ + e^{-i(2\omega_c+\Delta_i)t} a_c \sigma_i^-\big). \quad \text{(J3)}$$

The maximum probability using first-order time-dependent perturbation theory, with $g_1 = g_2 = g$ and $\hbar = 1$, can be calculated as follows. For $n_c > 0$,

$$\begin{aligned} P_{\max}(|n_c\rangle \to |n_c+1\rangle) &= \left[\max\left(-i\int_0^{t'} \langle n+1|V_I(t)|n\rangle_c dt'\right)\right]^2 \\ &= \left[\max\left(-i\int_0^{t'} \langle e_1(n+1)_c\phi_2|g e^{i(2\omega_c+\Delta_1)t} a_c^\dagger \sigma_1^+ |g_1 n_c \phi_2\rangle dt' \right.\right. \\ &\quad \left.\left. + \int_0^{t'} \langle \phi_1(n+1)_c e_2|g e^{i(2\omega_c+\Delta_2)t} a_c^\dagger \sigma_2^+ |\phi_1 n_c g_2\rangle dt'\right)\right]^2, \\ &= \left[\max\left(\frac{g\sqrt{n_c+1}}{2\omega_c+\Delta_1}\left(e^{i(2\omega_c+\Delta_1)t}-1\right) + \frac{g\sqrt{n_c+1}}{2\omega_c+\Delta_2}\left(e^{i(2\omega_c+\Delta_2)t}-1\right)\right)\right]^2 \\ &= \left[-g\sqrt{n_c+1}\left(\frac{1}{\omega_c+\Delta_1/2} + \frac{1}{\omega_c+\Delta_2/2}\right)\right]^2, \end{aligned} \quad \text{(J4)}$$

with $\Delta_i \ll \omega_c$, an order of magnitude estimate for the maximum probability of occupation of $n_c > 1$ is

$$P_{\max}(|n_c\rangle \to |n_c+1\rangle) \sim \left(\frac{g}{\omega_c}\right)^2. \quad \text{(J5)}$$

Figure 14 shows transition pathways to higher excited states of the cavity that involve lowest order processes in the perturbative energy nonconserving terms V_I. It is easy to see that a first-order process in V_I is required to populate the second and third excited states of the cavity, and a second-order process V_I is required to populate its fourth excited state. Using Eq. (J5) and $g/\omega_c = 0.01$, the probabilities for population of the higher excited states of the cavity are found to be

$$P_{\max}(|2_c\rangle) \sim 10^{-4}, \quad \text{(J6)}$$

$$P_{\max}(|3_c\rangle) \sim 10^{-4}, \quad \text{(J7)}$$

$$P_{\max}(|4_c\rangle) \sim 10^{-8}. \quad \text{(J8)}$$

More generally, for $\Delta_i \ll \omega_c$, the probability of occupation the nth excited state of the cavity can be estimated as

$$P_{\max}(|n_c\rangle) \sim \left(\frac{g}{\omega_c}\right)^{2\lfloor n/2 \rfloor}. \quad \text{(J9)}$$

When $\Delta_i \not\ll \omega_c$, higher cavity levels allow for virtual-coupling pathways formed by the energy nonconserving terms, but the levels themselves are never appreciably populated. While Eq. (J4) suggests that a large and negative Δ_i can increase the probability that higher levels are populated, it is countered by the suppressive role large detunings play in

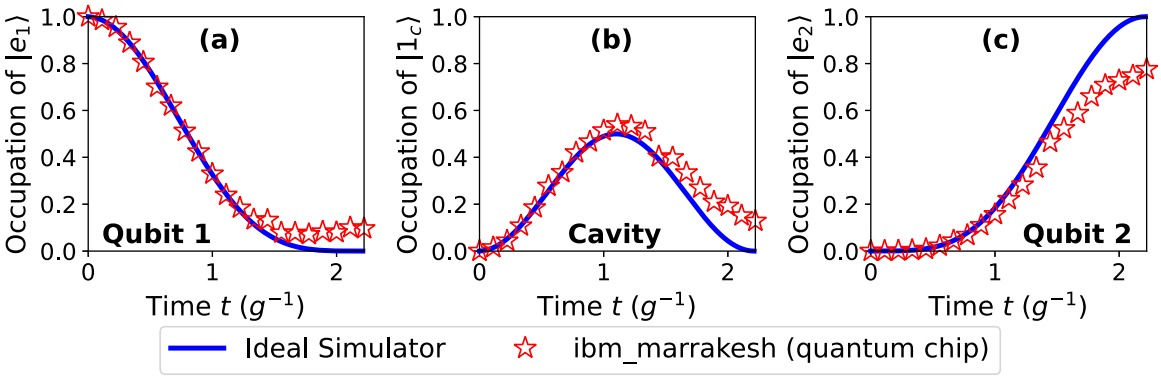


FIG. 15. Comparison of simulations on the ideal simulator vs ibm_marrakesh, one of IBM's quantum processors, for the resonant transfer of the quantum state from Qubit 1 to Qubit 2 via the cavity over a time $T = \pi/\sqrt{2}g$ across 20 steps, corresponding to a time step $\delta t \approx 0.1\, g^{-1}$. Panels (a), (b), and (c) show the evolution of the occupations of Qubit 1, cavity, and Qubit 2, respectively, as a function of time. The blue lines correspond to the ideal simulation, and the red stars correspond to simulation on ibm_marrakesh.

the coupling strength of the energy conserving terms, which scale as g/Δ.

APPENDIX K: SIMULATING RESONANT STATE TRANSFER ON NISQ HARDWARE

We evaluate the performance of our quantum circuit on readily available NISQ hardware, ibm_marrakesh [51], which is one of the IBM Heron r2 quantum processors. Figure 15 shows the evolution of the occupations of the qubits and the cavity as a function of time during the resonant transfer of the quantum state from Qubit 1 to Qubit 2 via the cavity, with $g_1 = g_2$ and $g/\omega_c = 0.01$. The blue lines are results from the ideal classical simulator and the red stars are those from ibm_marrakesh. The time evolution data from ibm_marrakesh is obtained by performing simulations for incremental durations, and measuring the qubits at the end of each simulation to obtain the state of the system at each time t. There is a close agreement between the two simulation modalities for about half the duration of the simulation, after which the processor's results deviate. This deviation could be due to several reasons. Imperfections in gate fidelity, particularly that of two-qubit gates, results in a trade-off between Trotter step size and circuit depth that can result in errors, particularly in longer simulations. For our simulations on the processor, we empirically observed that the maximum fidelity of ∼75% was obtained with a number of steps $r = 20$. This number is incidentally also obtained from the expression $r_{\text{optimal}} = 2(g_1\Delta_1 + g_2\Delta_2 + g_1g_2)^2T^4/m\epsilon_{2\text{qubit}}$, which is derived by minimizing a naive model of the combined error, $E_{\text{combined}} \equiv E_{\text{Trotter}} + E_{\text{gate}}$, with respect to r, where $E_{\text{Trotter}} = (g_1\Delta_1 + g_2\Delta_2 + g_1g_2)^2T^4/r^2$ [based on Eq. (F4)], and $E_{\text{gate}} = mr\epsilon_{2\text{qubit}}$ (m is the number of two-qubit gates per step and $\epsilon_{2\text{qubit}} \approx 0.003$ is the two-qubit gate infidelity on ibm_marrakesh).

As noted, such a model is naive and could possibly serve to provide an initial estimate of r. In general, when simulating on shared platforms that are not optimized for our model, suboptimal qubit allocation and circuit execution on a shared platform can result in further errors that are difficult to quantify. The results are expected to improve with optimized hardware settings or on dedicated platforms.

[1] H. J. Kimble, The quantum internet, Nature (London) **453**, 1023 (2008).
[2] L.-M. Duan, M. D. Lukin, J. I. Cirac, and P. Zoller, Long-distance quantum communication with atomic ensembles and linear optics, Nature (London) **414**, 413 (2001).
[3] L. Childress, J. M. Taylor, A. S. Sørensen, and M. D. Lukin, Fault-tolerant quantum communication based on solid-state photon emitters, Phys. Rev. Lett. **96**, 070504 (2006).
[4] I. Aharonovich, D. Englund, and M. Toth, Solid-state single-photon emitters, Nat. Photon. **10**, 631 (2016).
[5] D. D. Awschalom, R. Hanson, J. Wrachtrup, and B. B. Zhou, Quantum technologies with optically interfaced solid-state spins, Nat. Photon. **12**, 516 (2018).
[6] R. J. Schoelkopf and S. M. Girvin, Wiring up quantum systems, Nature (London) **451**, 664 (2008).
[7] S. Haroche and J. Raimond, *Exploring the Quantum: Atoms, Cavities, and Photons* (Oxford University Press, Oxford, 2006).
[8] E. Hagley, X. Maître, G. Nogues, C. Wunderlich, M. Brune, J. M. Raimond, and S. Haroche, Generation of Einstein-Podolsky-Rosen pairs of atoms, Phys. Rev. Lett. **79**, 1 (1997).
[9] T. Frey, P. J. Leek, M. Beck, A. Blais, T. Ihn, K. Ensslin, and A. Wallraff, Dipole coupling of a double quantum dot to a microwave resonator, Phys. Rev. Lett. **108**, 046807 (2012).
[10] D. Englund, B. Shields, K. Rivoire, F. Hatami, J. Vučković, H. Park, and M. D. Lukin, Deterministic coupling of a single nitrogen vacancy center to a photonic crystal cavity, Nano Lett. **10**, 3922 (2010).
[11] S.-B. Zheng and G.-C. Guo, Efficient scheme for two-atom entanglement and quantum information processing in cavity QED, Phys. Rev. Lett. **85**, 2392 (2000).
[12] C.-P. Yang, S.-I. Chu, and S. Han, Quantum information transfer and entanglement with SQUID qubits in cavity QED: A dark-state scheme with tolerance for nonuniform device parameter, Phys. Rev. Lett. **92**, 117902 (2004).

[13] D. Rosseau, Q. Ha, and T. Byrnes, Entanglement generation between two spinor Bose-Einstein condensates with cavity QED, Phys. Rev. A **90**, 052315 (2014).

[14] K. Wódkiewicz and J.H. Eberly, Markovian and non-Markovian behavior in two-level atom fluorescence, Ann. Phys. **101**, 574 (1976).

[15] J. R. Ackerhalt and J. H. Eberly, Quantum electrodynamics and radiation reaction: Nonrelativistic atomic frequency shifts and lifetimes, Phys. Rev. D **10**, 3350 (1974).

[16] H. J. Kimble and L. Mandel, Resonance fluorescence with excitation of finite bandwidth, Phys. Rev. A **15**, 689 (1977).

[17] P. Knight and P. Milonni, The Rabi frequency in optical spectra, Phys. Rep. **66**, 21 (1980).

[18] B. R. Mollow, Power spectrum of light scattered by two-level systems, Phys. Rev. **188**, 1969 (1969).

[19] J. D.-R. C. Cohen-Tannoudji and G. Grynberg, *Atom-Photon Interactions, Basic Processes and Applications* (John Wiley & Sons, Inc., New York, 1992).

[20] R. Loudon, *The Quantum Theory of Light*, edited by C. Press (Oxford University Press, England, 1983).

[21] J. Preskill, Quantum computing in the NISQ era and beyond, Quantum **2**, 79 (2018).

[22] B. Fauseweh, Quantum many-body simulations on digital quantum computers: State-of-the-art and future challenges, Nat. Commun. **15**, 2123 (2024).

[23] A. J. Daley, I. Bloch, C. Kokail, S. Flannigan, N. Pearson, M. Troyer, and P. Zoller, Practical quantum advantage in quantum simulation, Nature (London) **607**, 667 (2022).

[24] K. Bharti, A. Cervera-Lierta, T. H. Kyaw, T. Haug, S. Alperin-Lea, A. Anand, M. Degroote, H. Heimonen, J. S. Kottmann, T. Menke, W.-K. Mok, S. Sim, L.-C. Kwek, and A. Aspuru-Guzik, Noisy intermediate-scale quantum algorithms, Rev. Mod. Phys. **94**, 015004 (2022).

[25] M. Ippoliti, K. Kechedzhi, R. Moessner, S. Sondhi, and V. Khemani, Many-body physics in the NISQ era: Quantum programming a discrete time crystal, PRX Quantum **2**, 030346 (2021).

[26] H. F. Fotso, S. S. Yuvarajan, V. Iglesias-Cardinale, and D. Hucul, Quantum computation approaches for modeling photon-mediated operations in quantum information processing, in *Optics and Photonics for Information Processing XIX*, edited by K. M. Iftekharuddin, A. A. S. Awwal, V. H. Diaz-Ramirez, and A. Márquez (SPIE, Bellingham, Washington, 2025), Vol. 13604, pp. 136040K.

[27] A. Warren, U. Güngördü, J. P. Kestner, E. Barnes, and S. E. Economou, Robust photon-mediated entangling gates between quantum dot spin qubits, Phys. Rev. B **104**, 115308 (2021).

[28] A. Warren, E. Barnes, and S. E. Economou, Long-distance entangling gates between quantum dot spins mediated by a superconducting resonator, Phys. Rev. B **100**, 161303 (2019).

[29] V. Srinivasa, J. M. Taylor, and J. R. Petta, Cavity-mediated entanglement of parametrically driven spin qubits via sidebands, PRX Quantum **5**, 020339 (2024).

[30] M. Benito, J. R. Petta, and G. Burkard, Optimized cavity-mediated dispersive two-qubit gates between spin qubits, Phys. Rev. B **100**, 081412 (2019).

[31] H. F. Fotso, Pulse-enhanced two-photon interference with solid state quantum emitters, Phys. Rev. B **100**, 094309 (2019).

[32] H. F. Fotso, A. E. Feiguin, D. D. Awschalom, and V. V. Dobrovitski, Suppressing spectral diffusion of emitted photons with optical pulses, Phys. Rev. Lett. **116**, 033603 (2016).

[33] H. F. Fotso, Tuning spectral properties of individual and multiple quantum emitters in noisy environments, Phys. Rev. A **107**, 023719 (2023).

[34] H. F. Fotso, Controlling the emission and absorption spectrum of a quantum emitter in a dynamic environment, J. Phys. B: At. Mol. Opt. Phys. **52**, 025501 (2019).

[35] F. Beaudoin, A. Blais, and W. A. Coish, Hamiltonian engineering for robust quantum state transfer and qubit readout in cavity QED, New J. Phys. **19**, 023041 (2017).

[36] Y. Wang, T. Wang, and X.-Y. Zhu, Virtual photon-mediated quantum state transfer and remote entanglement between spin qubits in quantum dots using superadiabatic pulses, Entropy **26**, 379 (2024).

[37] M. H. Goerz, F. Motzoi, K. B. Whaley, and C. P. Koch, Charting the circuit QED design landscape using optimal control theory, npj Quantum Inf. **3**, 37 (2017).

[38] J. Zhou, Y. Hu, Z.-Q. Yin, Z. Wang, S.-L. Zhu, and Z.-Y. Xue, High fidelity quantum state transfer in electromechanical systems with intermediate coupling, Sci. Rep. **4**, 6237 (2014).

[39] N. Amgain, M. Rahman, U. Arshad, F. R. Consuegra, E. Sayahi, and I. M. Mirza, Tripartite entanglement in multimode cavity quantum electrodynamics, Phys. Rev. A **112**, 042423 (2025).

[40] E. Baum, A. Broman, T. Clarke, N. C. Costa, J. Mucciaccio, A. Yue, Y. Zhang, V. Norman, J. Patton, M. Radulaski, and R. T. Scalettar, Effect of emitters on quantum state transfer in coupled cavity arrays, Phys. Rev. B **105**, 195429 (2022).

[41] V. Iglesias-Cardinale, S. S. Yuvarajan, and H. F. Fotso, Dynamics of many-emitter ensembles: Probing cooperative evolution with scalable quantum circuits, arXiv:2603.12563.

[42] J. Dijkema, X. Xue, P. Harvey-Collard, M. Rimbach-Russ, S. L. de Snoo, G. Zheng, A. Sammak, G. Scappucci, and L. M. K. Vandersypen, Cavity-mediated iSWAP oscillations between distant spins, Nat. Phys. **21**, 168 (2025).

[43] P. Harvey-Collard, J. Dijkema, G. Zheng, A. Sammak, G. Scappucci, and L. M. K. Vandersypen, Coherent spin-spin coupling mediated by virtual microwave photons, Phys. Rev. X **12**, 021026 (2022).

[44] I. I. Rabi, On the process of space quantization, Phys. Rev. **49**, 324 (1936).

[45] I. I. Rabi, Space quantization in a gyrating magnetic field, Phys. Rev. **51**, 652 (1937).

[46] M. A. Nielsen and I. L. Chuang, *Quantum Computation and Quantum Information*, 10th anniversary ed. (Cambridge University Press, Cambridge, England, 2010).

[47] B. Peng, Y. Su, D. Claudino, K. Kowalski, G. Hao Low, and M. Roetteler, Quantum simulation of boson-related Hamiltonians: Techniques, effective Hamiltonian construction, and error analysis, Quantum Sci. Technol. **10**, 023002 (2025).

[48] A. Javadi-Abhari, M. Treinish, K. Krsulich, C. J. Wood, J. Lishman, J. Gacon, S. Martiel, P. D. Nation, L. S. Bishop, A. W. Cross, B. R. Johnson, and J. M. Gambetta, Quantum computing with Qiskit, arXiv:2405.08810.

[49] T. N. Ikeda, H. Kono, and K. Fujii, Measuring Trotter error and its application to precision-guaranteed Hamiltonian simulations, Phys. Rev. Res. **6**, 033285 (2024).

[50] A. Gilchrist, N. K. Langford, and M. A. Nielsen, Distance measures to compare real and ideal quantum processes, Phys. Rev. A **71**, 062310 (2005).

[51] IBM Quantum, 2026, https://quantum.cloud.ibm.com/.

[52] M. Tavis and F. W. Cummings, Exact solution for an *n*-molecule—Radiation-field Hamiltonian, Phys. Rev. **170**, 379 (1968).

[53] A. Dey, Correlating two qubits via a common cavity, Phys. Rev. A **111**, 043705 (2025).

[54] P. Gupta and C. M. Chandrashekar, Optimal quantum simulation of open quantum systems, arXiv:2012.07540.

[55] J. Van Damme, S. Massar, R. Acharya, T. Ivanov, D. Perez Lozano, Y. Canvel, M. Demarets, D. Vangoidsenhoven, Y. Hermans, J. G. Lai, A. M. Vadiraj, M. Mongillo, D. Wan, J. De Boeck, A. Potočnik, and K. De Greve, Advanced CMOS manufacturing of superconducting qubits on 300 mm wafers, Nature (London) **634**, 74 (2024).

[56] D. Zueco, G. M. Reuther, S. Kohler, and P. Hänggi, Qubit-oscillator dynamics in the dispersive regime: Analytical theory beyond the rotating-wave approximation, Phys. Rev. A **80**, 033846 (2009).

[57] D. Layden, First-order Trotter error from a second-order perspective, Phys. Rev. Lett. **128**, 210501 (2022).